REFLECT DELIVERABLE D1.3

Summary of gas solubility and degassing kinetics (type A)

Photo: Alper Baba, Izmir Institute of Technology

Summary:

This report describes the activities performed within Task 1.3 "Summary of gas solubility and degassing kinetics (type A)" until the end of month 39 of the REFLECT project. Two series of experiments have been carried out that assess the degassing process of type A geothermal fluids respectively in bulk and porous media. This has resulted in an improved understanding of the process and the associated physical phenomena by utilizing experimental equipment and data analysis tools specifically created for this task.

Authors:

Chris Boeije, Pacelli Zitha and Anne Pluymakers, Delft University of Technology

Title:	Summary of gas solubility and degassing kinetics (type A)
Lead beneficiary:	TUD
Other beneficiaries:	
Due date:	31 March 2023
Nature:	Public
Diffusion:	e.g. all Partners, WP-partners
Status:	Final
Document code:	REFLECT_D.1.3
DOI:	10.48440/gfz.4.8.2023.003
License information:	CC-BY-4.0
Recommended citation:	Boeije, C.S., Zitha, P.L.J., Pluymakers, A.H.M., *The H2020 REFLECT project: Deliverable 1.3 - Summary of gas solubility and degassing kinetics (type* A)*, GFZ German Research Centre for Geoscience; DOI: 10.48440/gfz.4.8.2023.003
ORCID:	Pacelli Zitha 0000-0002-1725-7000) Anne Pluymakers 0000-0001-9476-421X
Related Data:	Data associated with this publication are available from the following repository: "REFLECT deliverable 1.3: Summary of gas solubility and degassing kinetics (type A)", https://doi.org/10.4121/29de09ed-1b71-4bd1-b4ee-347a9481c34e

Revision history	Author	Delivery date	Summary of changes and comments
Version 01	CB	09.03.2023	Initial draft
Final version	CB	30.03.2023	Addressed comments from WP partners

Approval status				
	Name	Function	Date	Signature
Deliverable responsible	Chris Boeije		30.03.2023	
WP leader	Andrew Kilpatrick		29/03/23	
Project Coordinator	Simona Regenspurg		12.3.2023	

This document reflects only the author's view and the European Commission is not responsible for any use that may be made of the information it contains.

TABLE OF CONTENTS

1 EXECUTIVE SUMMARY

Geothermal fluids are often saturated with gasses such as CO_2 and N_2. Production of these fluids results in a pressure drop towards the extraction well. This disturbs the state of equilibrium of the geothermal water with its dissolved components, which can lead to the formation of free gas bubbles. The free gas can cause various problems such as corrosion of the facilities and increased levels of mineral scaling. The gas bubbles also take up space inside the pores of the reservoir rock, thereby limiting the ability for the water to flow. As this reduction occurs mainly near the extraction well it can reduce production of geothermal waters substantially.

The objective of this task (1.3) is to investigate the conditions under which free gas bubbles begin to form in a geothermal well or reservoir for hot fluids. To this end two different series of degassing experiments are performed to investigate bubble formation in bulk and porous media respectively. Bulk experiments were done using a high-pressure visual cell that was constructed specifically for this project. Depressurization experiments of gas-water mixtures were performed where a high-speed camera was employed to capture images of the process along with monitoring of the pressure and temperature. An image analysis routine was used that allows determining the pressure at which free gas bubbles begin to form and the rate of bubble formation during the depressurization process. Experiments performed within this task focus on mixtures of water and CO_2 as this is one of the most common gases in geothermal waters that is often present in high concentrations. For comparison, few experiments have been performed using nitrogen instead of CO_2. Various aspects that affect the bubble formation process were investigated, notably, the temperature of the mixture, the initial pressure and the rate of depressurization. Under moderate conditions, decent agreement was found between experimental results and the theoretical bubble point pressure, although deviations are observed at higher temperatures. Lower than expected bubble point pressures were found for experiments starting out with CO_2 in its supercritical state.

To assess the impact of degassing on flow in porous media, a series of coreflood (i.e. flow through rock cores) experiments was carried out. Here the aim was to determine the conditions under which degassing starts and quantitatively assess any associated permeability decrease. Tapwater containing dissolved carbon dioxide was injected into either a Bentheimer (2.3 D) or Berea (140 mD) sandstone core under different conditions. Initial experiments at 30 °C and pressure up to 50 bars showed that the pressure at which the first free gas is observed agrees with the theoretical bubble point. The free gas bubbles cause a permeability decrease of a factor 2 to 5 in the high permeability Bentheimer sandstone core, whereas in the low permeability Berea core, a reduction in permeability up to a factor 10 was observed. However, the pressure below which degassing starts is the same for both rock types. Increased deviations from theory are found when using higher temperatures.

2   DESIGN OF A HIGH PRESSURE VISUAL CELL

The first step of this project is the design and construction of a high pressure visual cell that can be used in degassing experiments. The cell is designed for monitoring the formation of free gas bubbles, specifically under conditions that are representative for the production of hot geothermal waters. That is, it needs to be to withstand high pressure and temperature and high levels of brine salinity. The initial design criteria for the cell were pressures up to 500 bar, temperatures up to 500 °C and suitable for use with a 1.5 M $CaCl_2$ + 2 M NaCl brine. During these experiments the cell is filled with a gas-liquid mixture at a certain pressure and subsequently heated to the desired temperature. Thereafter the cell is depressurized in a controlled manner.

At some point during this process, free gas bubbles can exsolve from the gas-liquid mixture. These experiments are aimed at finding the conditions when the gas exsolution starts and the rate of bubble formation. Therefore, two fully transparent sapphire windows are installed in the cell that allow for monitoring of the inner volume of the cell using a high-speed camera and a uniform light source. To prevent any corrosion of the cell due to contact with the high-salinity brine, the cell's surfaces are made out of titanium. A technical drawing showing a vertical cross section of the cell indicating its various components is shown in Figure 1 along with an isometric CAD drawing. A list of the different parts of the cell is given in Table 1. Note that the original design was commissioned to function up to 500 bar and 500°C, but the delivered product did not meet design specifications. Testing showed that safe operating conditions were limited to 200 bar and 200 °C. Therefore, these limits were used in the experiments within this project. A photograph showing the assembled cell is given in Figure 2.

Pressure and temperature need to be monitored during the depressurization process. Four Speed-bite fittings (Parker Autoclave Engineers) can be connected to the housing of the cell (cf. Figure 3). These are used to connect in- and outlet tubing along with a pressure transducer and thermocouple.
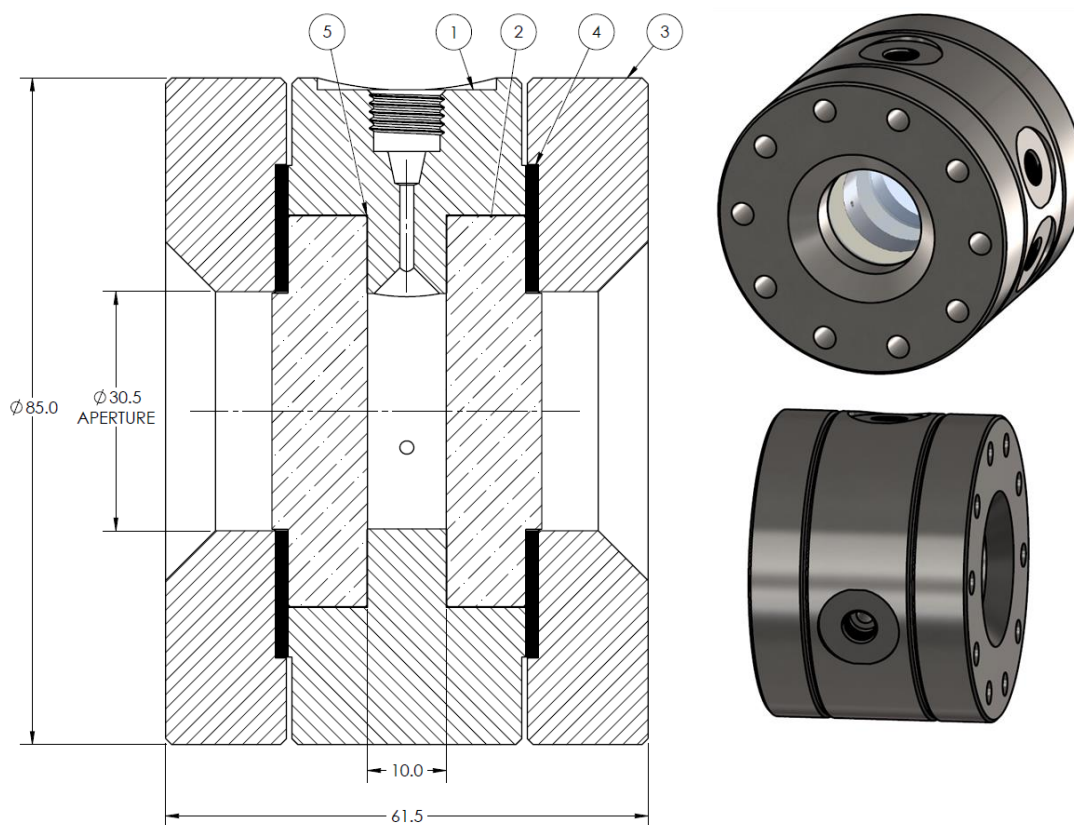
Figure 1: Left: Technical drawing of cell's vertical cross section (dimensions in mm) and Right: Isometric views of the cell

Table 1: Overview of the components of the high-pressure visual cell

Number	Description
1	Titanium cell housing
2	Sapphire window
3	Titanium flange
4	PTFE gasket
5	PTFE spacer shim
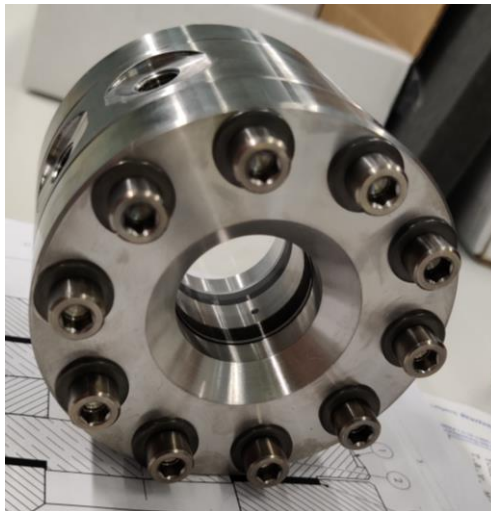
Figure 2: Photograph of the assembled visual cell

Figure 3: Front view of the cell's internal housing showing the outlines of the Speed-Bite fittings

3 HIGH SPEED IMAGING OF DEGASSING KINETICS OF CO_2-WATER MIXTURES

ABSTRACT
The exsolution of gas molecules from gas-liquid mixtures plays a significant roles in a wide range of applications from industrial process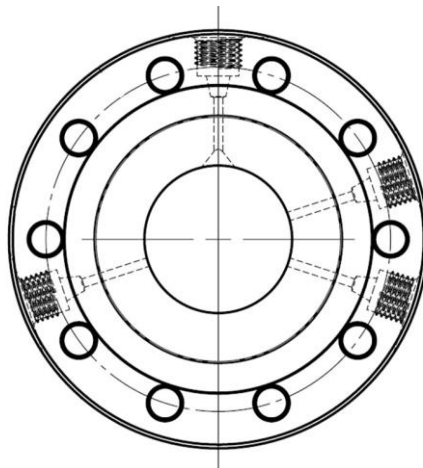es such as metal casting to subsurface flow of oil or geothermal waters. This study aims to improve the understanding of the conditions under which free gas bubbles start forming in CO_2-water mixtures. The bubble point pressure was determined under various different conditions like the temperature and initial pressure of the mixture along with other parameters such as the bubble growth rate.
A series of depressurization experiments at high pressures and temperatures (up to 100 bar and 100 °C) is performed using a pressure cell that allows for visual monitoring of the degassing process. Bubble formation during the depressurization process is recorded using a high-speed camera paired with a uniform light source along with a pressure transducer and thermocouple. Image analysis allows for determination of the bubble point pressure and rate of bubble formation.
For CO_2 in its gaseous state and at moderate temperatures, decent agreement between experimental results and the theoretical bubble point pressure is found, although significant deviations are observed at elevated temperatures. More pronounced differences in bubble point are observed for mixtures starting out at high pressures where CO_2 is a supercritical fluid, which lead to lower than expected bubble point pressures.

3.1 INTRODUCTION

Degassing is a process where free gas bubbles nucleate from a fluid containing dissolved gases. Bubbles form due to a change in the equilibrium conditions in the mixture that affect the gas solubility, such as a change in pressure or temperature (Barták, 1990; Kumzerova and Schmidt, 2002). In addition, degassing can also occur by exsolution of gas through a liquid-gas interface (without bubbling), as is the case in carbonated beverages(Liger-Belair et al., 2015).

3.1.1 Applications of degassing

Degassing of fluids plays a role in a variety of industrial and natural processes on a large range of scales, ranging in scale all the way from microfluidic devices to subsurface flows in reservoirs and volcanoes. In microfluidic systems, degassing can lead to trapping of air bubbles

whenever fluids are pumped, which can block flow paths or sensor surfaces(Cho et al., 2019; Karlsson et al., 2013). Since here bubbles have the same dimensions as the flow channels, the liquid flow is limited or blocked entirely, because of surface tension(Meng et al., 2006). This can also cause increased flow-induced shear stress(Park et al., 2021), which can be damaging when used in setups involving delicate materials such as living cells. During metal casting, e.g. for aluminum production, hydrogen bubbles may become trapped in the melt causing metal to become porous, which is detrimental for its mechanical properties(Gyarmati et al., 2021; Puga et al., 2011). A common practice to prevent this is to degas the molten metal using ultrasonic actuation. This increases diffusion of gas through the melt to the free gas bubbles, thereby increasing their size and allowing them to rise through the liquid and dissipate(Eskin et al., 2015; Eskin, 2015). Degassing is essential for foam injection molding. In this process, a gas-polymer mixture is injected into a mold at high pressure and then fills the cavity by reducing the pressure and allowing the gas to expand and fill the void. Pressure and injection speed govern the bubble nucleation and growth mechanisms and thus the structure of the foamed parts(Shaayegan et al., 2016; Wang, 2022; Xu et al., 2013). Degassing has several implications in oil production. For one, free CO_2 bubbles can cause more favorable conditions for the precipitation of calcium carbonate scale. In a hydrogeochemical model up to twelve times more scaling was found for scenarios that incorporate degassed CO_2 compared to scenarios that do not(Fu et al., 2013). Under oil well conditions, CO_2 degassing is estimated to be responsible for 60 to 90% of carbonate scaling(Cosmo et al., 2019), leading to production problems(Garven, 2015). The exsolution of gas can also improve oil recovery as the gas reduces the hydrostatic pressure in the well thereby lifting the other fluids to the surface (gas lift)(Groth et al., 2009; Ivannikov et al., 2003). Furthermore, gas exsolution from carbonated water is found to lead to oil mobilization, which can also increase recovery(Qin et al., 2021).

Degassing also occurs during the production of geothermal brines. These are typically saturated with calcium ions and thus calcite precipitation also occurs in geothermal wells, similarly to oil wells(Arnórsson, 1989; Stefánsson et al., 2016; Taweelarp et al., 2021). Corrosion is also expected to occur in both geothermal and oil wells, for chemically active gases such as CO_2 or H_2 (Pátzay et al., 1998). Another issue for geothermal water production is that the formation of free gas can cause reduction of the water relative permeability in reservoirs thus limiting the production rate of these waters. The Groß Schönebeck field in Germany saw a 93% decrease in its productivity index from June 2011 to November 2013 for which the presence of free gas in the near-well region was considered a likely cause(Blöcher et al., 2016). Surveys of CO_2 degassing in soils have also been used to explore the potential of various sites in Italy(Chiodini et al., 2007; Frondini et al., 2009) and the Canary Islands(Rodríguez et al., 2021) to contain geothermal resources and in the Los Humeros field in Mexico, regions of high degassing were found to indicate the presence of high-permeability faults(Peiffer et al., 2018). On large time scales, degassing is also known to cause significant CO_2 emissions into the atmosphere(Sbrana et al., 2020; Shen et al., 2011; Taweelarp et al., 2021), but can also enhance microbial life in the subsurface(Bornemann et al., 2020). Similar methods were also employed to analyze the rates of degassing from the Mount Etna volcano(Aiuppa et al., 2006) and assess its magmatic reservoir pressure(Caracausi et al., 2003).

3.1.2 Objectives of study

This study aims to provide high quality data and analysis on the emergence of free CO_2 bubbles from fluids along with the development of the bubble population during a depressurization process, under temperature, pressure and concentrations relevant to low temperature geothermal water production. Most of the literature relevant to degassing of geothermal brines is related to the solubility of gases in these brines. Various sets of solubility measurement data are available in literature for CO_2 solubility in NaCl and $CaCl_2$ solutions(Carvalho et al., 2015; Lara Cruz et al., 2021; Zhao et al., 2015) or focus on the modeling of such systems(dos Santos et al., 2021; Duan and Sun, 2003; Li et al., 2014). However, the bubble nucleation process and bubble population development at conditions relevant to geothermal water production have not been studied extensively thus far.

The main research topics that are addressed here are the dependency of the bubble point pressure on the various initial conditions and the parameters that control the evolution of the bubble population. To this end, a series of experiments is performed where a high pressure CO_2-water mixture is depressurized inside a visual cell. A high-speed camera is used to visually monitor the process of bubble nucleation and simultaneously pressure and temperature are logged.

3.1.3 Background theory

Within this study, degassing is considered in the form of gas exsolution leading to bubble nucleation as this is the most relevant to the production of geothermal waters. Two bubble nucleation mechanisms are commonly distinguished: homogeneous vs. heterogeneous nucleation(Delale et al., 2002). Heterogeneous nucleation occurs on impurities on surfaces or specks of dust which function as nucleation sites for bubbles to form. Homogeneous nucleation happens in pure liquids where such nucleation sites are not present making it more difficult for bubbles to form and liquids can be reduced in pressure considerably below the saturation vapour pressure without any bubble formation(Meadley and Escobedo, 2012). Heterogeneous nucleation is considered the dominant bubble formation mechanism in this study due to the presence of surface imperfections within the experimental apparatus.

The solubility of CO_2 in water is proportional to the partial pressure of CO_2 and follows Henry's law. Thus for the production of geothermal waters, where the pressure reduces as it flows towards the production well, the solubility threshold can be exceeded leading to a supersaturated state. If the gas cannot exsolve from the solution through an existing gas-liquid interface, bubbles may start to nucleate. To start the heterogeneous nucleation process, surface imperfections with a large radius of curvature are required to overcome the required energy barrier. This critical radius of curvature is a function of the interfacial tension between liquid and gas and the concentration of CO_2 in the liquid(Liger-Belair, 2019). As the pressure is reduced further, the degree to which the solution is supersaturated (i.e. its supersaturation ratio) increases controls, which leads to an increase of the rate at which bubbles are formed(Uzel et al., 2006).

3.2 MATERIALS AND METHODS

Experiments performed in this study focus on the formation of free CO_2 bubbles during depressurization mimicking the changes in pressure experienced in a geothermal well. The experiments were done at temperatures ranging from 20 to 100 °C, where the elevated temperatures are representative of low enthalpy geothermal sites. This section describes the experimental setup used in this study and outlines the steps taken both during the experiments and the subsequent data analysis approach.

3.2.1 Experimental setup

Figure 4 shows a schematic of the experimental setup that is used in these experiments. The setup consists of the following components: a Chandler Engineering Quizix QX6000 dual piston pump allows for pumping water at high pressure. A Proserv Prolight 002990 titanium transfer vessel with a magnetic stirrer is used for creating gas-liquid mixtures. A stainless steel, high-pressure visual cell with two borosilicate sight glasses on either side to allow for visualization of the flow inside. These sight glasses are circular and the aperture available for visualization is 30 mm in diameter. This 30 mm is also the diameter of the cell's cylindrical internal volume and it has a depth of 11.6 mm. Fluid inlet and outlet are located at bottom and top of the cell respectively (cf. Figure 5). A LED light source is installed to allow for uniform illumination of the cell's inner volume. A heating spiral is wrapped around the cell such that it can be heated up to the desired temperature in combination with a PID thermo-controller.

A Photron FASTCAM Mini UX100 camera is installed in front of the cell's window for high speed imaging of the contents of the cell. This camera is used here at a rate of 500 frames per second. The camera is paired with a Nikon AF-S Nikkor 18-105 mm. This lens is meant for use with consumer Nikon digital cameras that have a larger sensor than the one present in the Photron camera used here. This means its image circle is considerably larger than is required to fill the frame, which means that light fall-off in the corners of the image is virtually non-existent. The lens is used at a focal length of approximately 55 mm and an aperture of 1:3.5. These settings allow for the camera to be placed some distance away from the cell window, which is necessary for use at elevated temperature.

A Druck PTX 611 pressure transducer is connected to the cell to monitor the pressure during the experiments at a frequency of 100 Hz. Two thermo-couples are connected to the cell as well: one for connecting to the thermo-controller and one to a data acquisition PC. The system's pressure is controlled using a Mity Mite S-91W gas loaded back pressure regulator combined with a nitrogen gas bottle. A needle valve within the back-pressure tubing allows for releasing the pressure in a controlled and reproducible manner. A hardware switch is connected to both the camera and the data acquisition PC, which is used to synchronize the captured images from the camera and the pressure and temperature logs.
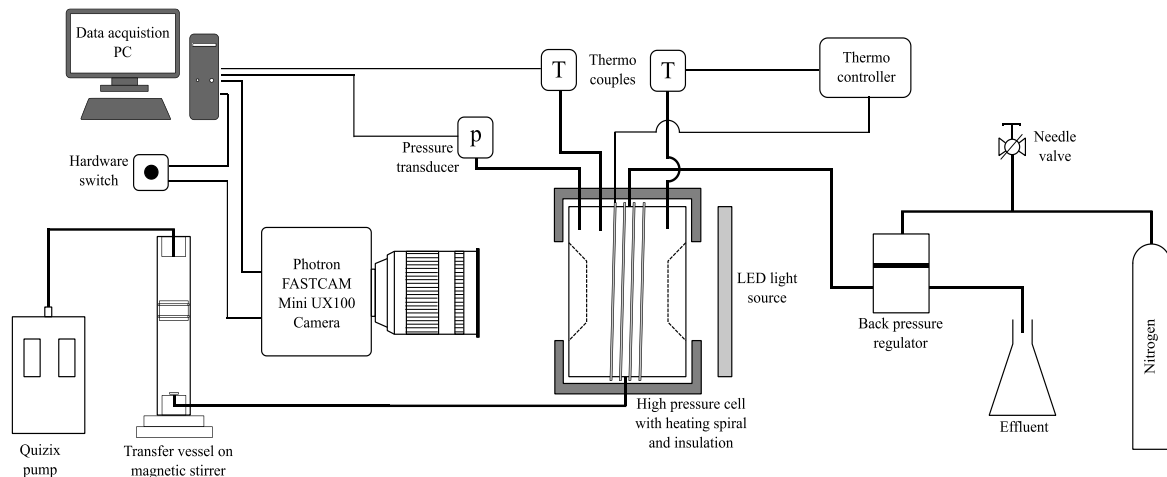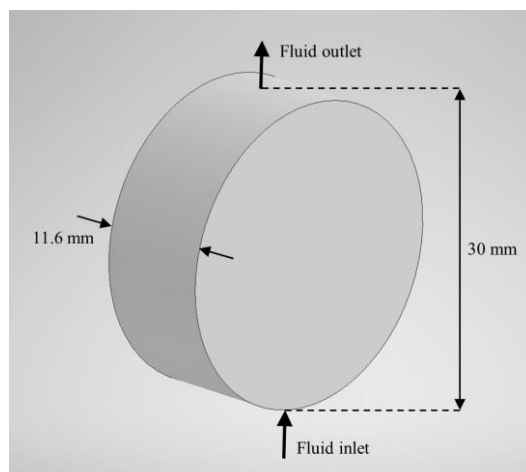
Figure 4: Schematic of experimental setup

Figure 5: Cylindrical internal volume of pressure cell with fluid inlet and outlet indicated along with relevant dimensions

3.2.2 Experimental procedure

Prior to starting the experiments, DI water and CO_2 are premixed in the desired proportions and pressure in the transfer vessel. The desired quantity of CO_2 is injected into the water filled vessel by means of a Bronkhorst ELFLOW mass flow controller. The fluids are then homogenized using a magnetic stirrer while maintaining a constant pressure in the pressure using the injection pump, which allows the CO_2 to dissolve in the water. This constant pressure is maintained overnight after which the injection pump is switched off. Pressure is still monitored and a constant pressure in the vessel implies that all of the injected CO_2 has dissolved in the water. The visual cell is initially pressurized by filling it with DI water. Subsequently, the water-CO_2 mixture can be pumped from the transfer vessel into the cell, displacing the initial DI water. To ensure that the cell contains only the CO_2-water mixture at the appropriate concentration, the total volume of water-CO_2 mixture that is pumped into the

cell is 5 times the cell volume. During elevated temperature experiments, the cell is then heated to the desired temperature using the heating spiral.

Once the desired conditions are reached, the depressurization process can commence by opening a needle-valve in the back-pressure system. This allows for a controlled and reproducible manner of reducing the system pressure. At a certain point during this process, the first free CO_2 bubbles emerge from the solution. The pressure at which this occurs is the bubble point pressure. The bubble formation process is captured in a series of images using the high-speed camera. Around 18500 images are captured for each experiment at a resolution of 640x480 pixels. When the 30 mm sight glass fills the entire image, this means that the pixel size is approximately 62 microns (= 30 mm / 480 pixels), which is also the minimum bubble size that can be identified. The number of images and the rate of capture means that the total duration of each experiment is around 37 seconds, which is enough for the full depressurization process to be performed. The image capturing sequence is ended by pressing a hardware switch, which simultaneously sends a pulse to the data acquisition PC to allow for synchronization of images with the pressure and temperature data.

3.2.3 Data analysis methods

The main result from each experiment is a set of images that show the emergence and evolution of bubbles during the degassing process. An image analysis routine was developed using the MATLAB Image Processing Toolbox to identify individual bubbles and their properties such as size and growth rate. Since the images captured during the experiment and the pressure log are synchronized, the bubble data from the analyzed images are combined with the pressure data to determine at which pressure bubbles are formed during the degassing process.

The image analysis method is the following: first the background image (i.e. the image at the start of the experiment before bubble formation) is subtracted resulting in net images with bubbles showing up as regions of high intensity. A global intensity threshold is used to convert these net images to a binary format. Individual bubbles are identified in these images using MATLAB's regionprops function, which uses pixel connectivity to determine whether pixels are part of the same region. Single pixel regions could be caused by digital noise that can impact the results thus only regions of two or more pixels are considered in the remainder of the analysis.

A distinction is made between trapped bubbles that are growing on the cell's surfaces and free flowing bubbles inside the cell. This is done by comparing consecutive images with each other. If there is no difference in the position of a bubble compared to its position five frames earlier, that bubble is considered trapped. Finally, the number of bubbles (i.e. individual regions) are counted on every image and can be plotted as a function of pressure. The pressure at which the first bubble emerges from the solution is the bubble point pressure. Further analysis of the bubbles on the images allows for assessing the bubbles' growth rate by computing the equivalent diameter using $D_{eq} = \sqrt{4A/\pi}$, where A is the measured bubble area. Both the average growth rate of the bubbles due to gas expansion as a result of the depressurization and the growth of ascending individual bubbles due to gas diffusion to the bubble were investigated.

3.2.4 Overview of experiments

Several experiments were performed in this study with a range of different initial conditions. The conditions that were varied include initial pressure, temperature and gas concentration. All experiments here were carried out using DI water as the aqueous phase. Experiments performed at ambient temperature only consist of the depressurization process whereas elevated temperature experiments also contain the heating stage prior to depressurization. Table 2 shows an overview of the experiments that were carried out within this study. All of these were performed by dissolving CO_2 in water at a certain pressure and monitoring the degassing that takes place due to depressurization. The initial mixing of water and CO_2 in the transfer vessel is performed at ambient temperature after which the fluid mixture is pumped into the cell and heated. This means that for high pressure experiments using CO_2, the CO_2 is actually initially liquid and undergoes a phase transition to a supercritical state during the heating stage ($p_{crit,CO2}$ = 73.8 bar, $T_{crit,CO2}$ = 31.0 °C). The state of the CO_2 at the beginning of the depressurization process is stated explicitly in the table.

Table 2: Overview of experimental conditions for elevated temperature experiments.

Initial pressure [bar]	Temperature (°C)	Initial CO$_2$ concentration [mol/L]	Phase state of dissolved CO$_2$
30	20, 40, 60, 100	0.200	Gas
50	20, 40, 60, 100	0.200	Gas
100	20, 40, 60, 100	0.200	Liquid or supercritical
30	20	1.01[*]	Gas[**]

[*]This is a fully saturated solution, i.e. this is the maximum CO_2 that can be dissolved at this pressure

[**]This is a series of experiments using different initial fluids to assess its influence on the degassing process

The main parameter studied here is the occurrence of the first free bubble as a function of the temperature and initial pressure of the mixture (see subsection 3.3.1 of the Results). Further details of the degassing process, such as the evolution of bubble size and influence of other experimental parameters, like the rate of depressurization are discussed in subsection 3.3.2. A general discussion of the bubble formation process is presented in subsection 3.3.3.

3.3 RESULTS AND DISCUSSION

3.3.1 Bubble point pressure

Most of the experiments discussed here were performed using solutions of CO_2 in brine at a concentration of 0.2 mol/L. This concentration was chosen for two main reasons. Firstly, it is significantly lower than the fully saturated solution at ambient temperature. This ensures that no bubbles form during the heating stage for most of the experiments, which could obscure the interpretation of the depressurization process. Secondly, this concentration is representative for geothermal reservoirs, for which typically CO_2 concentrations range from 0.0114 to 0.227 mol/L(Henley et al., 1984). For certain fields CO_2 concentrations as high as 0.772 mol/L were found(Haizlip et al., 2016). Experiments done at much higher CO_2 concentration (1.01 mol/L) are discussed in section B. These experiments were performed to assess the influence of the initial fluid in the visual cell on the degassing process.

Figure 6 compares the bubble point pressure, i.e. the pressure at which the first bubbles are observed, for the experiments with initial CO_2 concentration of 0.2 mol/L. During these experiments the temperature and the initial pressure were varied. The data publication associated with this document that is mentioned in the beginning of this chapter contains an example of the image analysis method for the experiment starting at 100 bar and 100 °C.
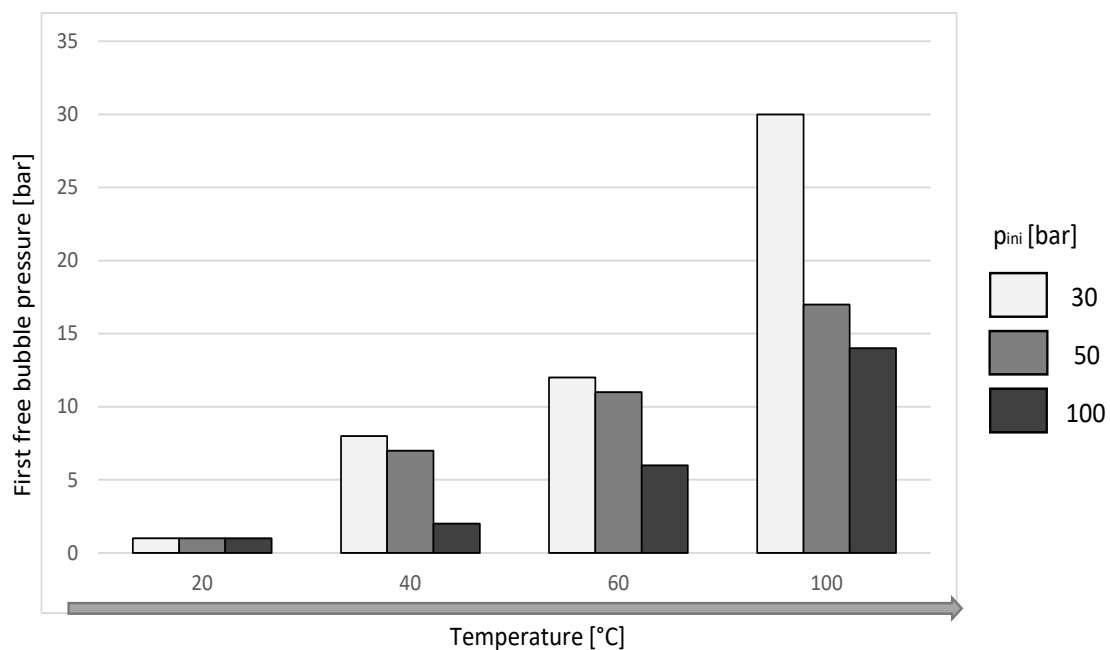

Figure 6: First free bubble pressure for the CO_2 depressurization experiments vs. temperature for an initial CO_2 concentration of 0.2 mol/L at three initial pressures, 30, 50 and 100 bar as indicated by the bars' grayscale

In all experiments except the one at 30 bar experiment at 100 °C, the solubility limit for CO_2 in water was not exceeded during the heating stage so that no free gas bubbles were formed prior to the depressurization process. For the 30 bar/100 °C experiment, bubbles were formed during the heating sequence, implying that for this experiment the CO_2 concentration exceeded the CO_2 solubility limit. This means that in this case, free gas bubbles are present

right from the start of the experiment. The solubility of CO_2 at elevated temperature can be estimated using Henry's law in combination with the Van 't Hoff equation(Smith, 2007). The latter equation accounts for the temperature dependence of the gas solubility and is given in equation   (1).

$$H(T) = H^0 \exp\left[\frac{-\Delta_{sol}H}{R}\left(\frac{1}{T} - \frac{1}{T^0}\right)\right] \qquad (1)$$

where H^0 is Henry's constant at 25 °C, which for CO_2 is $3.4 \cdot 10^{-2}$ mol/(L · atm) and $-\Delta_{sol}H$ refers to enthalpy (i.e. the H is not equivalent to Henry's constant) with $\frac{-\Delta_{sol}H}{R}$ equal to 2400 K for CO_2. The solubility diagram, represented as contours of constant solubility for gaseous CO_2-water mixtures, obtained with equation 1 is shown in Figure 7. The solubility of CO_2 in water was calculated for many values of pressure and temperature using the Van 't Hoff equation (Eq. 1). Subsequently, a contour fitting routine was employed to determine the iso-solubility contours that are given in the figure. The 0.2 mol/L contour is given in bold in this figure as this is the concentration used in most of these experiments, which is why theoretically this is where the first free gas bubble is expected. At pressures below this contour the CO_2 solubility is less, so gas exsolution is expected. The phase diagram of CO_2 is superimposed on this figure to underscore the fact that the equation applies for gaseous CO_2. The experiments performed here are also shown in this figure as lines starting at the initial conditions (indicated by the symbol ●) and ending at the bubble point pressure (indicated by the symbol ■).
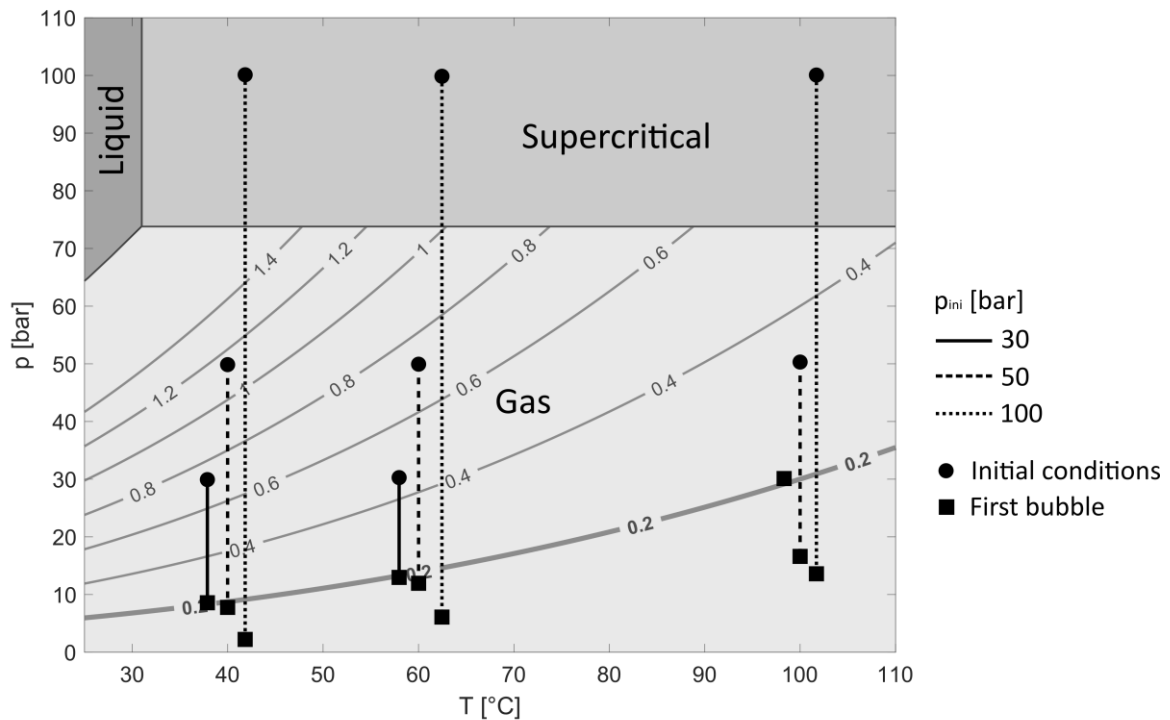
Figure 7: Iso-solubility contours for CO_2 dissolved in brine[mol/L] as a function of temperature and pressure superposed on the CO_2 phase diagram. The 0.2 mol/L contour is shown as a thicker line, because this is the concentration that was used in these experiments. The vertical lines in the figure indicate the depressurization path for the experiments conducted in this study.

The figure shows that the solubility of CO_2 at 30 bar and 100 °C is nearly equal to 0.2 mol/L, explaining why a few free gas bubbles were already formed during the heating stage. The equation thus explains why no free gas bubbles were formed during the heating stage for the other experiments, that are performed either at higher initial pressure or lower temperature, both of which lead to an increased CO_2 solubility.

The depressurization path for the 30 bar/40 °C experiment shows the first bubble forming around 8 bar, which coincides with the 0.2 mol/L contour implying that for these conditions the Van 't Hoff equation accurately predicts the bubble point pressure. This is not the case for the experiment that start out under supercritical conditions (p_{ini} = 100 bar). Despite using the same 0.2 mol/L concentration as in the lower pressure experiments (p_{ini} = 30 bar), the first bubble is observed at pressures that are significantly below the 0.2 mol/L contour. This is the case for all three investigated temperatures. However, for all experiments the bubble point pressure increases with temperature. This is in good agreement with the prediction of the Van 't Hoff equation that CO_2 solubility decreases as temperature increases.

The low-pressure experiments (p_{ini} = 30 bar) showed reasonable agreement with Van 't Hoff theory in terms of predicting when the first free gas bubble was formed. The same cannot be said for the experiments with p_{ini} = 100 bar (cf. Figure 7), where consistent lower bubble point pressures were found than predicted by the Van 't Hoff equation. Here we look at the depressurization process for these experiments (p_{ini} = 100 bar, T = 40, 60 and 100 °C) in greater detail. No bubbles are formed during the heating process even when heating to 100 °C, thus

no nucleation points were present at the start of the depressurization process for any of these experiments. For the 100 °C experiment, this explains why there is no immediate degassing taking place as was the case for the experiment at lower pressure (p_{ini} = 30 bar, T = 100 °C). However, there are distinct differences in the bubble point pressure which indicates that some additional physics are involved here. Some possible explanations for this are discussed in the next section.

One of the major changes between experiments is that CO_2 is in its supercritical state for these higher pressure experiments ($p_{crit,CO2}$ = 73.8 bar, $T_{crit,CO2}$ = 31.0 °C). Thus a phase change occurs during the depressurization process from supercritical to a gaseous state for the CO_2, which significantly affects the bubble nucleation process. Interestingly, there is no optical change to any of the images at the pressure where the phase change takes place: the images remained free of bubbles until much lower pressures. This shows that even though the optical properties of water with dissolved supercritical CO_2 vs dissolved gaseous CO_2 are the same, the physics of how degassing takes place is nonetheless affected.

During most of the experiments performed here, there is a delay (that is, a required reduction of pressure) of 2 to 3 bar between the nucleation of the first free gas bubble and the rapid linear increase in the number of bubbles. This delay is of relevance to the application in geothermal reservoirs where large amounts of free gas bubbles can contribute to blocking reservoir pore space as is assumed to have happened at the Groß Schönebeck reservoir in Germany(Blöcher et al., 2016).

3.3.2 Influence of other parameters on the degassing process

There are a number of other parameters that may influence the bubble formation process. Some of these, such as the analysis of locations where bubbles form and the evolution of bubble size, are investigated through further examination of the previously obtained data. Some additional experiments have been performed to examine the influence of other parameters, such as the influence of the depressurization rate and the cell's materials. All of these parameters are discussed in this section.

Cumulative bubble intensity

To check if bubbles are formed randomly or are predominantly formed in distinct locations, such as in small scratches on the housing or windows of the cell, we have checked cumulative intensity maps of different image series. These are normalized summations of the black and white conversions of the images. Locations where bubbles are present most of the time show up as regions of high intensity on these maps, thus allowing identification of regions of intense degassing. Figure 8a-b show the resulting intensity maps for the experiments using (a) p_{ini} = 100 bar, T = 100 °C and (b) p_{ini} = 30 bar, T = 40 °C. These two different conditions were chosen to see whether pressure and temperature affect the locations of bubble nucleation.
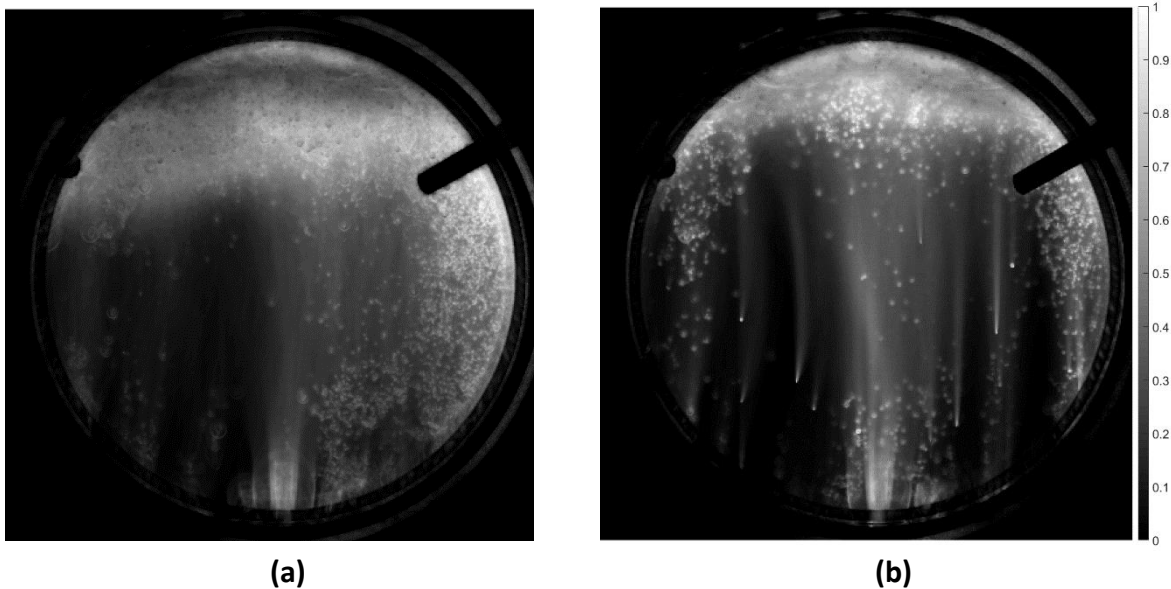
Figure 8: Normalized cumulative intensity maps of the experiments using 0.2 mol/L CO_2 using the indicated initial pressure and temperature. (a) p_{ini} = 100 bar, T = 100 °C, (b) p_{ini} = 30 bar, T = 40 °C

The only two high intensity regions that show up in both intensity maps are the top and bottom of the visual cell. Both these sites contain sharp edges, which could and do act as a nucleation sites for bubbles. Comparing the glass sides of the cell there are no bubble nucleation regions which coincide in both experiments. However, in the map for lower initial pressure (30 bar/40 °C), distinct high intensity bubble trails are present. During a single experiment preferential regions of bubble nucleation can form, but those same regions do not necessarily carry over between experiments. Within one experiment, at some point the bubble size is such that the buoyancy force is greater than the wall friction, at which point the bubble detaches from the glass and rises in the cell. Some CO_2 from the bubble is left at the surface, and this acts as a nucleation point for the next bubble to form and thus the cycle repeats.

Influence of initial fluid on bubble formation
The presence and the number of initial nucleation points inside the visual cell was found to be one of the main parameters that controls the bubble formation. The 30 bar/100 °C experiment started degassing right from the start, because free gas bubbles were already present within the cell at the pressure and temperature the experiment started. These gas bubbles acted as nucleation points, where bubbles form and grow in size. This implies that using initial conditions where nucleation points, such as free gas is present can significantly affect the degassing behavior. To test this idea, a series of experiments were performed at ambient temperature using a 30 bar initial pressure where the initial fluid used to pressurize the cell was varied. The different initial fluids used here for cell pressurization are nitrogen (N_2) and water (H_2O). The premise is that when using gas as the initial fluid, these molecules adsorb onto imperfections on the cell's surface (windows and steel housing) and serve as points on which new, free gas bubbles can easily start to nucleate. On the other side of the spectrum, water is injected into the cell under vacuum to establish the least nucleation points. The

graphs labelled "H_2O" use water pumped into a vacuum in the cell, whereas graphs labelled "H_2O+" use water pumped into a cell containing air. In the latter case, residual air contributes to the number of bubble nucleation sites on the cell's surface, which affects its degassing process, and provides therefore an intermediate number of nucleation points (i.e. more nucleation points than for the "H_2O" experiments, but not as many as the "N_2" experiments). An overview of the results in terms of bubble point pressure and the maximum number of observed bubbles is given in Figure 9, where the initial fluid is indicated at the bottom of each bar in the graph. The number of bubbles is indicated here by the gray scale of the bar graphs with darker shades implying more observed bubbles. The quantity plotted here is the logarithm of the maximum number of bubbles ($\log(N_{b,max})$) observed within the single image during the degassing process.

This set of experiments is done using water that is fully saturated with CO_2, i.e. a concentration of 1.01 mol/L (Henry's Law). The concentration here is thus roughly 5 times higher than in the experiments discussed above. Water and CO_2 are mixed in the transfer vessel at the desired 30 bar pressure with sufficient CO_2 being fed into the vessel to fully saturate the water. The initial fluid on the bubble point pressure correlates well with the number of nucleation points. When using N_2 as the initial fluid, a bubble point pressure is found, which is significantly higher than the 14 bar in the experiments using water and ambient air as the initial fluid (H_2O+). An exception however is observed for water into a vacuum (i.e. the H_2O labelled bar in the figure), for which the bubble pressure is similar to the experiments that start with a nitrogen pressurized cell (26 bar). However, in this "H_2O" experiment, there was only a single bubble observed at this elevated pressure and throughout the process the number of bubbles remained rather low. Using gas as an initial fluid results in up to three order of magnitudes more bubbles compared to the experiment where water is used as an initial fluid. Results from these experiments are reproducible, with max 2 bar difference in the observed bubble point pressure and similar number of bubbles found. The stark contrast between the number of bubbles observed in the various experiments suggests also a mitigation option for subsurface operations that are hindered by degassing. Rendering a surface fully water-wet is shown here to have the potential to significantly reduce the effects of degassing in processes where free gas bubbles cause problems.
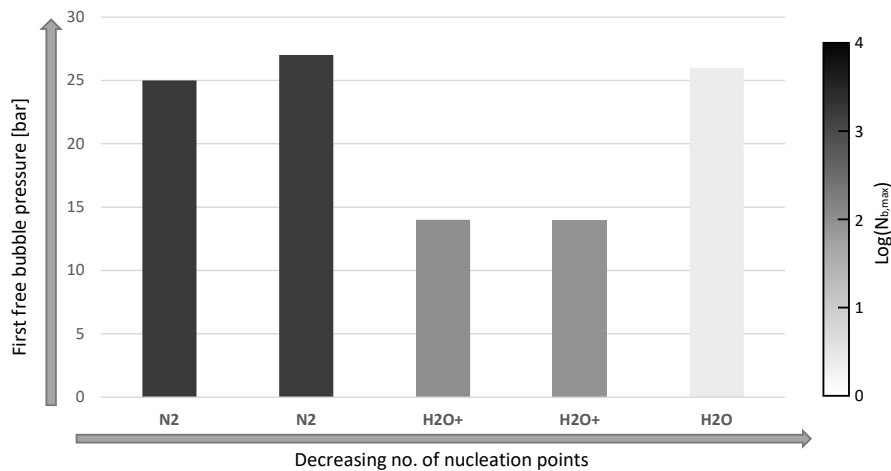
Figure 9: Pressure where the first free bubble occurs for CO_2 saturated water starting at 30 bar. Initial fluid used to pressurize the cell is given below each bar. Grayscale indicates the peak of the number of bubbles that is formed during the experiment.

Experiments using other pressure cell

The material and surface conditions of the visual cell (i.e. the presence of scratches on the glass or metal parts of the cell) are expected to impact the degassing process. A series of experiments was therefore carried out using another visual of similar dimensions as that used in the experiments discussed above, but made from different material. This cell's housing is made out of titanium and its windows are sapphire glass as opposed to the stainless steel and borosilicate glass used in the previous experiments. The experiments using the new cell were conducted with the 0.2 mol/L CO_2 concentration that was also used in the previous experiments. Temperatures of 40, 60 and 100 °C were investigated and initial pressures of 30 and 100 bar. Figure 10 shows a comparison in bubble point between the different cells under these conditions. For most experiments, only small differences are observed (~1 bar). The main exception is the 40 °C experiment using the old cell, which has a significantly lower bubble point compared to the new experiment. The trend that a lower bubble point is observed using a higher initial pressure is found in both sets of experiments though and is thus not considered to be caused by the cell's materials.
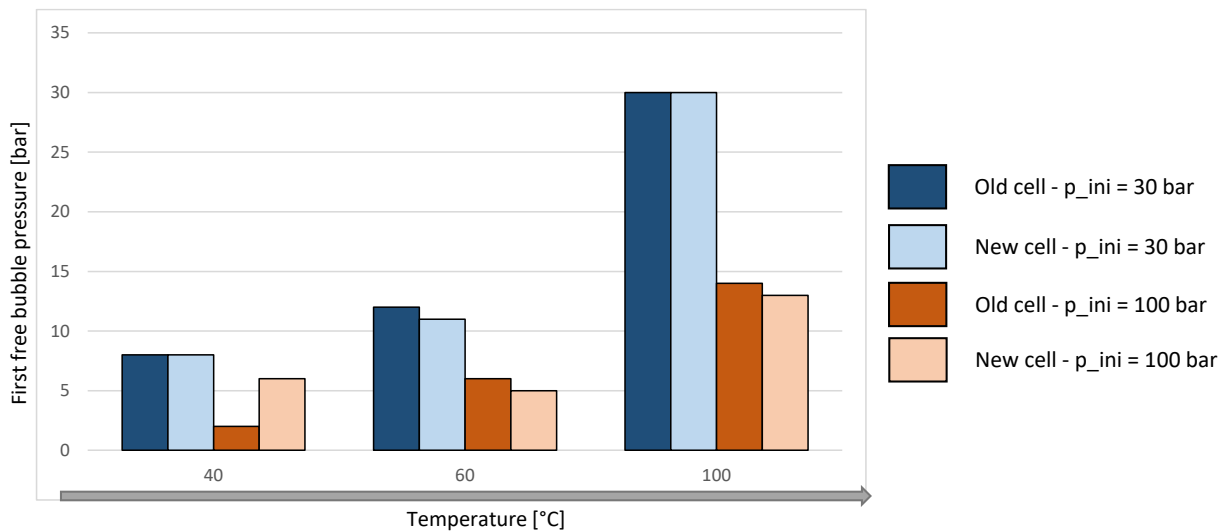
Figure 10: Comparison of the bubble point between the old and new cell for the indicated conditions

Lower rate depressurization experiments

A series of experiments was performed at a lower rate of depressurization to assess whether time-dependent kinetics such as the role of diffusion play a significant role in the bubble formation. In these experiments the depressurization process takes approximately three times longer than in the previous series while all other conditions were kept the same. The hypothesis here is that bubble formation is diffusion controlled. That is, CO_2 molecules need to diffuse from the solution to the bubble's surface, which can take time. Here we try to establish whether this time is of significance in the observed bubble points.

These experiments were performed using the titanium cell with sapphire windows and are thus compared with the previous set of experiments using the same cell. To maintain the same frame rate and resolution compared to the other experiments another camera was used here (Photron FASTCAM NOVA S6) that allows for extended recording time. A total of over 55000 images were captured for each experiment in this series. The focus here is on experiments with p_{ini} = 100 bar, because that's where the largest deviations were observed compared to solubility theory. Figure 11 shows the measured bubble points for both the high and low rates for depressurization. Some differences are present, the largest being the 3 bar difference found for the 100 °C experiment. However, there does not appear to be a clear trend in these differences, i.e. the lower rate experiments do not consistently lead to lower or higher bubbles point pressures. Therefore, it assumed that the observed differences are down to measurement errors rather than that they represent a real trend.
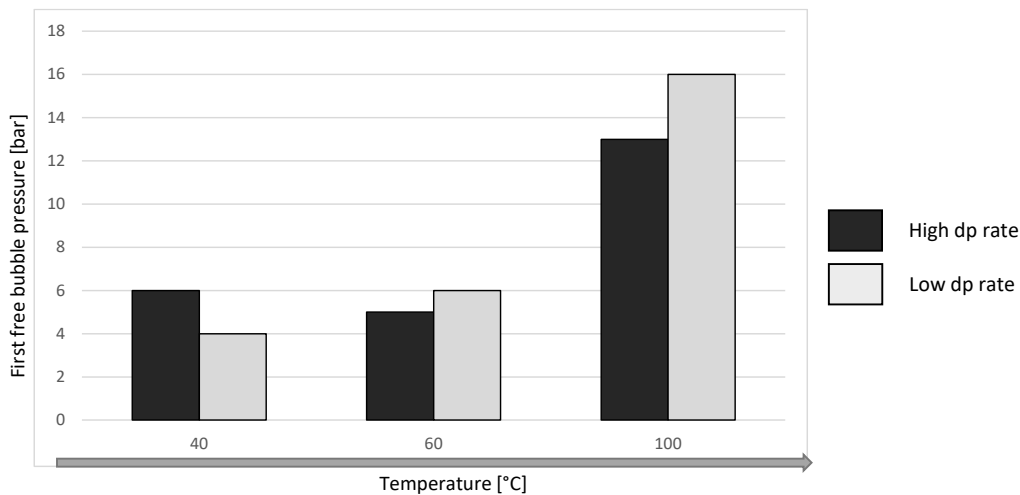
Figure 11: Comparison bubble points for high and low rates of depressurization ("dp rate")

Influence of equation of state on model prediction

For moderate temperatures, the bubble point pressure can be reasonably predicted using the Van 't Hoff equation, whereas at higher temperatures a larger deviation is found. A possible explanation for this is that the value of the term $\frac{-\Delta_{sol}H}{R}$ in this equation is incorrect. A value of 2400 K is used for creating the plots depicted here, but different values can be found in literature ranging from 2200 to 2900 K(Sander, 2015), which would alter the predicted solubility significantly. Other models using a different equation of state are also available. For comparison, here we consider the equation of state from Duan and Sun (2003) and see how that affects the predicted solubility. Figure 12 shows the iso-solubility contours for CO_2 in water as a function of the pressure and temperature based on the equation of state of Duan and Sun as opposed to the contours based on the Van 't Hoff equation in Figure 7. Experimental results showing the first observed free gas bubble for all the investigated cases are shown as symbols that vary depending on the initial pressure that was used in the experiment (p_{ini} = 30 bar (●), 50 bar (■) and 100 bar (▼)).
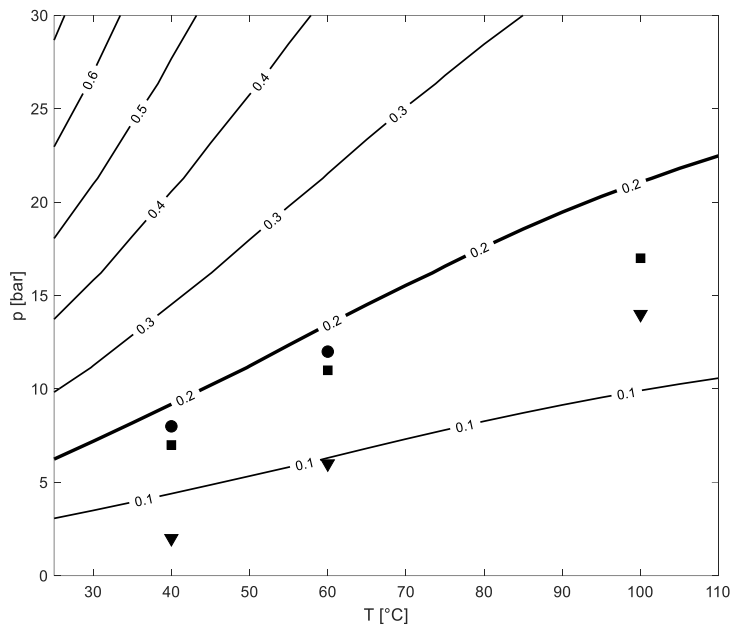
Figure 12: Iso-solubility contours of CO_2 in water [mol/L] based on a model using the Equation of State from Duan and Sun (2003). The 0.2 mol/L contour is given in bold as this is the concentration of CO_2 used in these experiments. Symbols correspond to the observed first free gas bubble during the depressurization experiments for p_{ini} = 30 bar (●), 50 bar (■) and 100 bar (▼).

The contours obtained using the equation of state from Duan and Sun are significantly different from those using the Van 't Hoff equation. The deviation between model prediction and the experiments in the high temperature regime is somewhat better using this equation of state. However, this improved model still does not predict the observed difference between experiments employing different initial pressure and thus different initial CO_2 phase.

Analysis of differences in bubble kinetics
A possible explanation for the variation in observed bubble point pressure between experiments with different initial pressure is that the kinetics of bubble formation differ. Different mechanisms during the bubble formation process are investigated here and assessments are made on their significance in explaining the observed variations. Two mechanisms contribute to bubble growth during the depressurization process: (a) bubble size increases due to gas expansion at lower pressure and (b) CO_2 mass transfer from the surrounding medium into the bubble. Mechanism (a) is studied here by analyzing the average bubble size throughout the degassing process. This is done by computing the equivalent diameter for each bubble as outlined in the methodology section of this manuscript. For bubbles with a short residence time in the cell, mechanism (b) is likely to be dominant due to the limited change in pressure. This mechanism is studied by analyzing the growth of individual bubbles as they ascend within the visual cell.

Evolution of average bubble size

Experiments with different initial pressures, but otherwise identical conditions were compared in terms of the average equivalent bubble diameter. This is calculated by summing the equivalent diameters for the individual bubbles and dividing by the number of bubbles within the image. Figure 13 shows the bubble growth during the two experiments at 100 °C (p_{ini} = 30 bar and 100 bar). Symbols (cross or square) represent the average equivalent diameter within a single image. To maintain a readable graph with a limited number of symbols not every captured image is shown here, but rather the obtained value for every 30th image along with a linear fit to the data for moderate pressures (i.e. below 15 bar) to emphasize the bubble growth behavior in this regime.
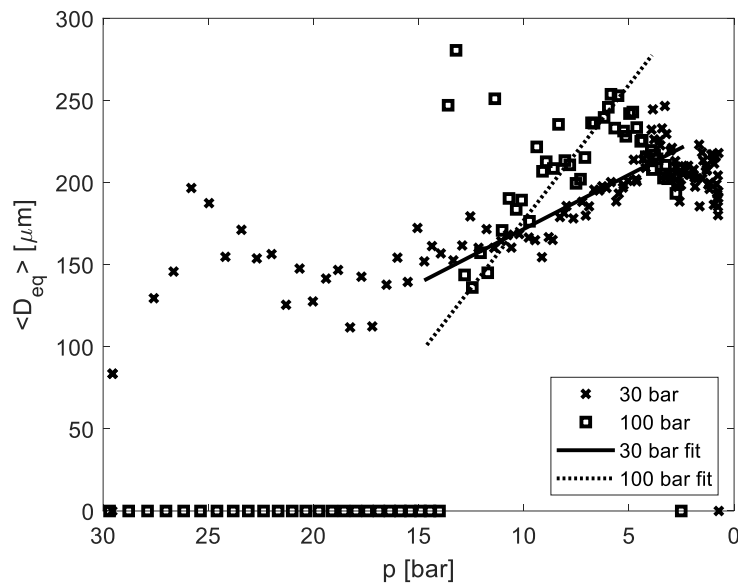

Figure 13: Comparison of average equivalent bubble diameter <D_{eq}> for the experiments at 100 °C and p_{ini} = 30 and 100 bar

At 30 bar, bubbles start forming right from the start, owing to the formation of bubbles during the heating stage. The average bubble size stays fairly constant for the first portion of the depressurization process. However, below ~15 bar, the average bubble size inside the cell increases linearly as the pressure decreases due to gas expansion. For the 100 bar experiment, bubbles are not present at the start, but only start forming at 14 bar. Below this pressure, a linear increase in bubble size is observed. In this pressure range, the rate of the bubble growth is higher for the 100 bar experiments as there is still more gas in solution compared to the 30 bar experiment at the same pressure where gas was lost during the heating stage. At low pressures (<5 bar) similar average bubble sizes are observed for both experiments.

Manual tracking of individual bubbles on images

In addition to variation in bubble size during the degassing process, another question concerns how individual bubbles grow as they ascend within the visual cell. To answer this question, we compare experiments having different initial pressures, at the same stage of depressurization i.e. when pressure reaches the same value, 10 bar. Several bubbles are tracked by eye as they

ascend within the cell in consecutive images. On this scale, bubble growth is not dominated by gas expansion due to pressure reduction, since the pressure barely decreases within the few analyzed images. Instead, the bubbles' surface acts as a nucleation site for itself causing dissolved CO_2 in the liquid to diffuse to the bubble which makes it grow(Shafer and Zare, 1991). Typically, bubbles in a supersaturated solution grow at a constant rate as they ascend through the liquid independent of their size(Zenit and Rodríguez-Rodríguez, 2018). Figure 14 shows an example series of black and white conversions of the images around 10 bar for the experiment at 100 °C with p_{ini} = 100 bar. There is a 10 ms interval between the consecutive images shown here to show a distinct rise of the bubbles between each image. The spots on the black background represent individual free gas bubbles. A number of bubbles has been given a certain color. This allows for individual bubbles to be tracked across multiple images as they ascend through the cell. For example, the red bubble in each of the images in the figure corresponds to the same bubble at different stages of its rise through the cell. The size of the colored bubbles is then analyzed by determining its area and corresponding equivalent diameter. Bubbles of various sizes are present within each image. Figure 15a, b and c show the bubble size for the five colored bubbles as they ascend through the visual cell with p_{ini} = 30, 50 and 100 bar respectively. The horizontal and vertical axes in these plots is the same for both experiments to allow for direct comparison. There is a significant margin of error for each bubble due to the limited resolution of the images. Therefore, the error is equal to the pixel size of the images, which is indicated by error bars in these images. Not all bubbles have the same size at the start of their rise through the cell, a range of different diameters is found for each experiment. However, within a single experiment, the bubbles' growth rate is found to be approximately constant. That is, within each experiment, the slope of each line graph is almost identical for all the bubbles observed here. The constant growth rate, independent of bubble size, is in agreement with previous studies(Liger-Belair, 2005; Zenit and Rodríguez-Rodríguez, 2018).This is the case for both the 50 and the 100 bar experiment and similar bubble diameter growth rates are found for both experiments of approximately $2.0 \cdot 10^3$ µm/s, i.e. there is a similar CO_2 mass transfer from the surrounding medium into the bubble at 50 and 100 bar. This cannot be said for the 30 bar experiment, which shows a considerably lower bubbles growth rate of around $5.8 \cdot 10^2$ µm/s. A likely cause for this is that for the 30 bar experiment, there were already bubbles forming during the heating stage of the experiment, which results in a lower CO_2 concentration in the liquid during the depressurization. As such, fewer CO_2 molecules can adsorb onto the bubbles' surface, limiting CO_2 mass transfer from bulk solution into the bubble.

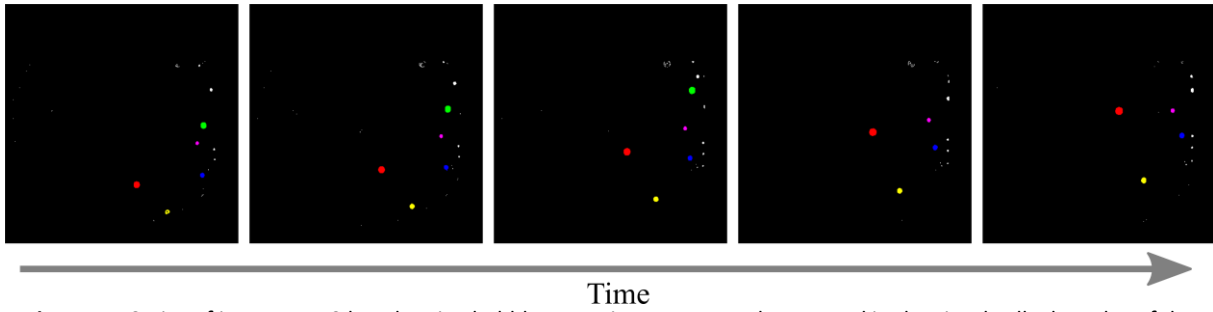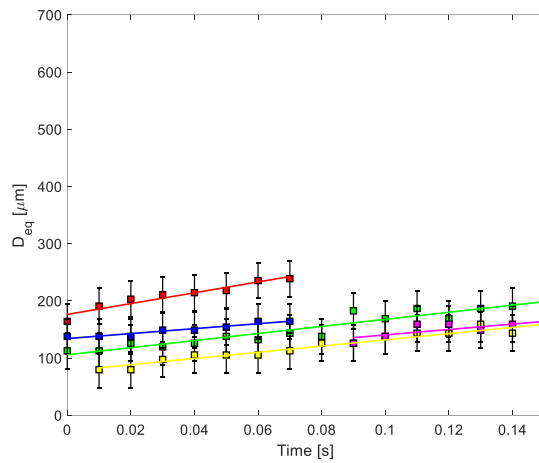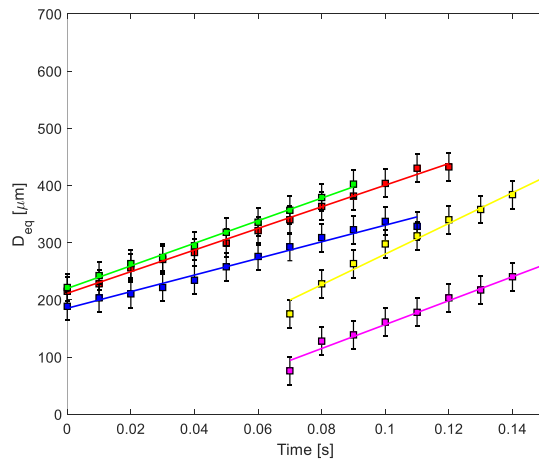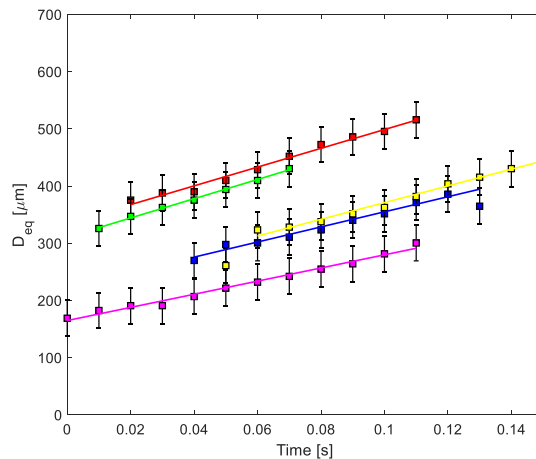**Figure 14:** Series of images at 10 bar showing bubbles at various stages as they ascend in the visual cell. The color of the bubble functions as a label and allows an individual bubble to be tracked across multiple images.

(a)

(b)

(c)

Figure 15: Bubble size vs. time, for five individual bubbles as they ascend in the visual cell at a pressure of 10 bar and 100 °C for (a) p_{ini} = 30 bar, (b) p_{ini} = 50 bar, (c) p_{ini} = 100 bar

3.3.3 A conceptual model of bubble formation during depressurization of CO_2-water mixtures

This section describes the process of CO_2 bubble formation during the depressurization process in a conceptual way. The various aspects and stages of the process are discussed along with parameters of influence. A schematic overview of the process is also presented in Figure 16.

For most of the experiments discussed here, the depressurization process starts with the CO_2-water mixture as a single homogenous phase. The CO_2 remains in solution until a certain threshold pressure is reached where the solution reaches supersaturation, thus free gas bubbles start to form (cf. Figure 16a). This 'bubble-point pressure' is dependent of temperature and of CO_2 concentration. Bubbles will first appear on the surfaces of the cell, because CO_2 molecules can accumulate in small scratches and rough patches on the surface(Shafer and Zare, 1991). After the initial bubble surface has formed, this surface then allows for more CO_2 molecules to adsorb onto the bubble, causing the bubble to grow. The bubble keeps growing on the surface until the buoyancy force of the bubble is large enough for the bubble to detach from the surface and rise through the liquid (Figure 16b).

Some CO_2 molecules are left on the wall in the location from which the bubble detached and this will be the site for a new bubble to form. The presence of nucleation sites is a key factor to determine final bubble density. The rising bubbles that have detached from the cell's surface will grow at a constant rate that is independent of their initial size (Figure 16c). However, the rate at which they grow is dependent on the CO_2 concentration that is still in solution, with higher concentrations causing a more rapid increase in bubble size.
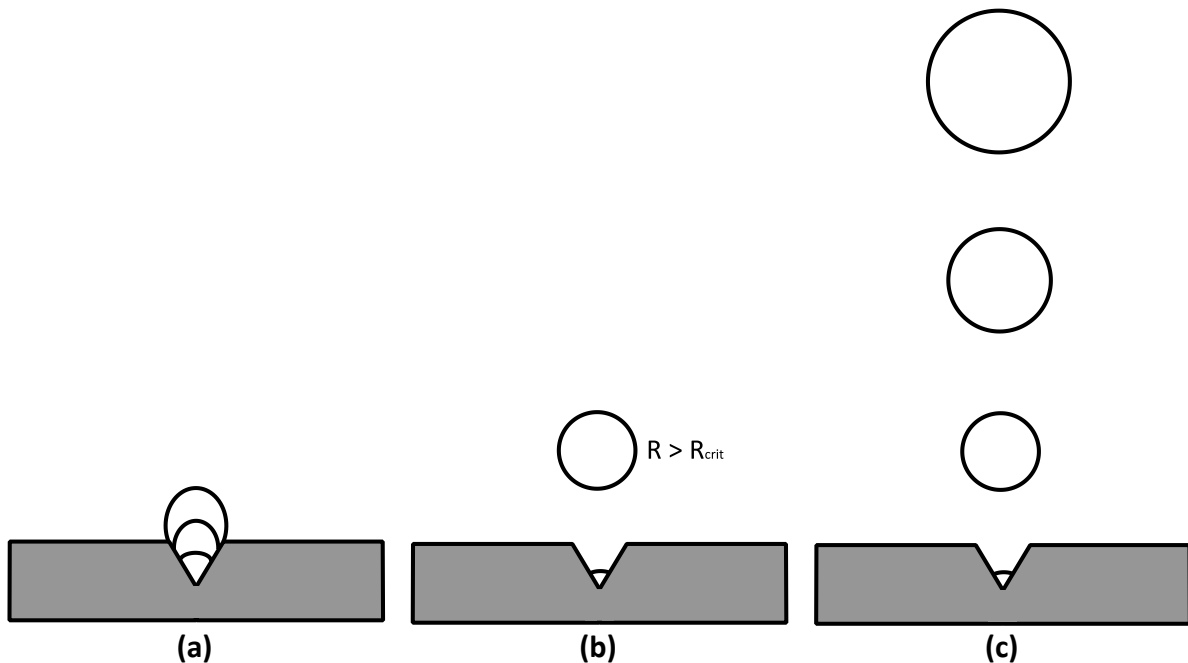
Figure 16: Schematic overview of the bubble growth process. (a) A bubble forms on a crack in the surface and starts to grow (various stages of the bubble's growth are depicted), (b) Once the bubble has grown larger than the critical radius it detaches and rises in the liquid leaving behind a small surface in the crack on which the next bubble starts growing, (c) As the bubbles rise through the liquid, dissolved CO_2 molecules will adsorb onto its surface thus leading to further bubble growth

At pressures and temperatures where CO_2 is in the gaseous phase, the pressure at which the first bubble forms can be predicted with reasonable accuracy at ambient temperature using either the Van 't Hoff equation or the equation of state of Duan and Sun. At elevated temperature, more significant deviations are found. A so far unexplained finding of this study is that the pressure where the first bubble forms is a function of the initial pressure (or initial phase). The experiment with p_{ini} = 100 bar with CO_2 in its supercritical state showed a bubble point between 6 and 16 bar lower than predicted, unlikethe experiment with p_{ini} = 30 bar, where the bubble point was within 2 bar of the prediction. Several possible explanations for this have been examined including repeat experiments using another visual cell and changing the rate of depressurization. Deviations in bubble point pressure up to 3 bar were found, but without a clear trend in the deviations.

Both the average bubble size throughout the depressurization process and the growth rate of individual bubbles in the experiments at 100 °C have been analyzed. Due to the formation of bubbles in the heating stage for the 30 bar experiment, bubbles start forming there throughout the entire depressurization process with the average bubble size increasing linearly throughout. For the 100 bar experiment, bubbles only form below 14 bar, but the average bubble size increases more rapidly below this pressure resulting in similar average bubble sizes at low pressure for both experiments. The bubble growth rates for individual bubbles were the same for the 50 and the 100 bar experiment. A much lower growth rate was found for the 30 bar experiment, but this can be attributed to the formation of bubbles during the heating stage of the experiment causing a lower concentration of CO_2 in the solution.

3.4 ADDITIONAL EXPERIMENTS USING NITROGEN GAS

Some additional experiments were performed using nitrogen gas dissolved in the water instead of CO_2 to see how these compare in terms of bubble formation rate and average size. These experiments are performed at ambient temperature at an initial pressure of 70 bar using a fully saturated solution. (Baranenko et al., 1990) report the solubility of nitrogen under various conditions. Interpolating their results to the conditions used here and converting units yields an initial nitrogen concentration of approximately 0.039 mol/L. This is significantly less than the solubility of CO_2 under the same conditions. Various different fluids were used to pressurize the cell to determine its effect on the bubble formation rate. This means that these experiments are similar to those performed using CO_2 at ambient temperature that were also carried out using a fully saturated solution as discussed in section 3.3.2. The pressurization fluids used here are helium (He), nitrogen (N2), water (H2O) and water injected into ambient air (H2O+). An overview of the bubble point pressure is given in Figure 17. The gray scale of the bars indicates the maximum number of bubbles that was observed in a single image during the degassing process. This figure clearly shows a clear correlation between the number of initial nucleation points and both the bubble point pressure and maximum number of bubbles. Starting out with a gas like helium or nitrogen results in formation of bubbles at higher pressures compared to experiments that start out with water. Differences of up to 25 bar were found in bubble point pressure when comparing different experiments. Also, the maximum number of bubbles observed when using a gas is orders of magnitude higher. The experiments starting out with water as the initial fluids only showed a very limited number of bubbles. This is in agreement with the experiments where CO_2 was used, which showed similar behavior.
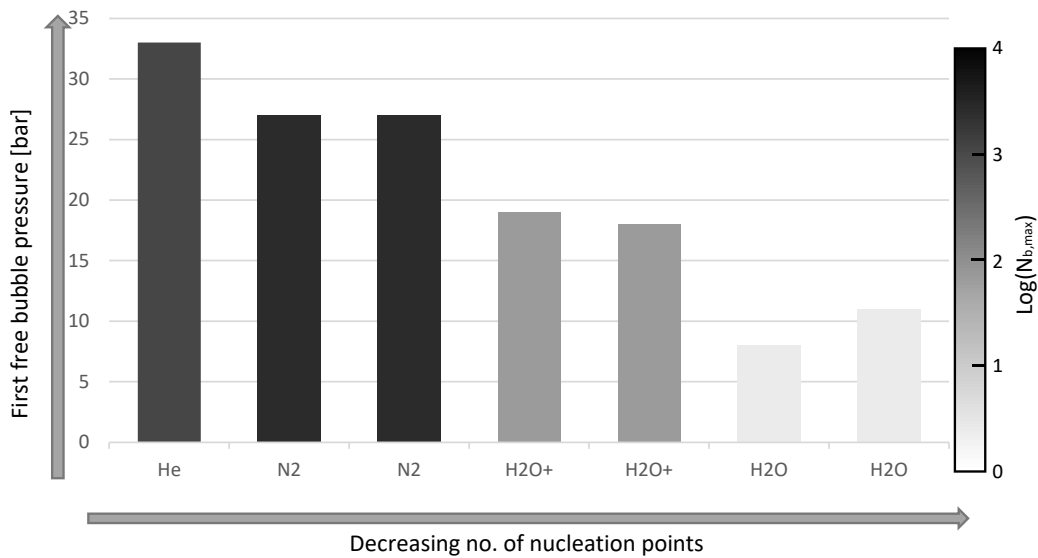
Figure 17: Pressure where the first free bubble occurs for N_2 saturated water starting at 70 bar. Initial fluid used to pressurize the cell is given below each bar. Grayscale indicates the peak of the number of bubbles that is formed during the experiment.

The average bubble size of the two experiments with the largest number of generated bubbles (i.e. using helium and nitrogen as the initial fluid) was also determined. The resulting bubble size as a function of the pressure is shown in Figure 18 for both experiments.

Figure 18: Comparison of average equivalent bubble diameter <D_{eq}> for the nitrogen experiments using helium (He) and nitrogen (N2) as initial fluids
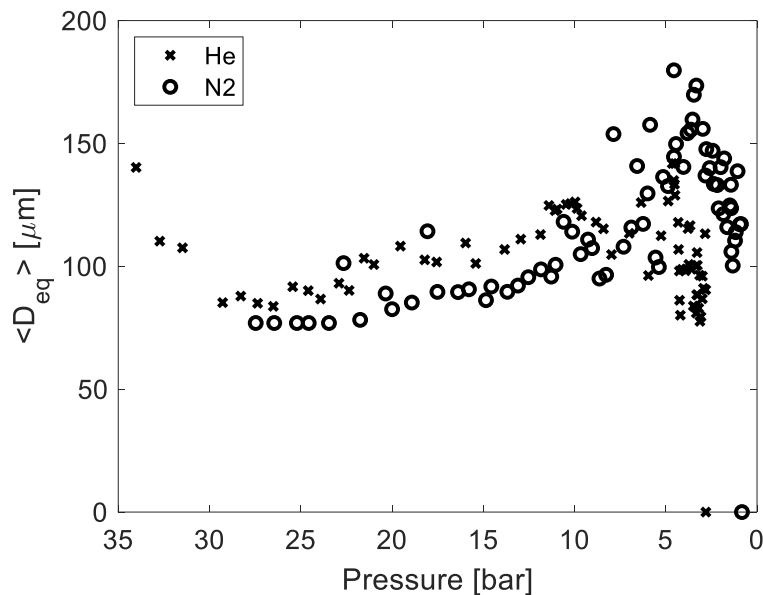
In both experiments, the average bubble size starts out fairly small (< 100 μm) and increases gradually as the pressure is reduced. When comparing the bubble size of nitrogen to that of CO_2 as shown in Figure 13, it can be observed that the nitrogen bubbles are significantly smaller (approximately 50% smaller average diameter) compared to CO_2 bubbles. This is likely caused by the reduced solubility of nitrogen compared to CO_2 meaning that fewer molecules need to gather together in order to form a bubble. The reduced solubility of nitrogen also implies that the total free gas release is limited compared to that of CO_2.

3.5 CONCLUSIONS AND RECOMMENDATIONS

- When CO_2 is in a gaseous state, the formation of the first free gas bubbles is in reasonable agreement with the Van 't Hoff equation, which dictates the solubility of gases at elevated temperatures.
- This is not the case for experiments at higher initial pressure (100 bar) that start out with CO_2 in a supercritical state. Here the bubble point pressure is consistently lower than the expected bubble point based on the Van 't Hoff equation.
- Higher temperatures lead to increased deviation from the Van 't Hoff theory. Better estimates can be established using other equations of state (e.g. Duan and Sun (2003)), but deviations still persist.
- At ambient temperature, the degassing process is heavily affected by the presence of nucleation sites, in terms of first bubble formed, and total bubble density, as observed for experiments with different initial fluids. For experiments with p_{ini} = 30 bar, up to 12 bar difference is found in bubble point pressure and up to three orders of magnitude in terms of the observed number of bubbles when comparing experiments with high and low number of initial nucleation sites.

- Several possible explanations have been investigated that could cause the dependency of the bubble point pressure, such as the bubble growth rate and the speed of depressurization. The sensitivity analysis on the physical parameters provided no clear indication that they could have a significant impact on the bubble point. This study only provides estimates of the extent to which each of the parameters affects the bubble point pressure. Additional, more quantitative analysis is recommended to fully understand the physics involved here. Results found in this study can serve as a starting point when setting operating conditions for geothermal water production. Naturally additional properties of the specific field (e.g. brine salinity) need to be taken into account to limit or prevent the occurrence of degassing.
- Additional experiments at ambient temperature using nitrogen gas instead of CO_2 also show the effect of the presence of nucleation sites during the degassing process. Similar to the CO_2 experiments, the number of bubbles can vary by three orders of magnitude and differences in the bubble point pressure of up to 25 bars were found when comparing experiments with high and low number of initial nucleation sites.

4 CO₂ DEGASSING OF GEOTHERMAL FLUIDS DURING CORE-FLOOD EXPERIMENTS

This chapter contains content that has been presented and published as: Boeije, C.S., Verweij, C., Zitha, P.L.J. and Pluymakers, A.H.M., "CO_2 degassing of geothermal fluids during core-flood experiments", presented at the European Geothermal Congress 2022, Berlin, Germany, 17 – 21 October 2022

ABSTRACT

The long-term performance of the reservoir is essential in order to ensure competitive life-cycle cost of the geothermal installations. Geothermal fluids are often saturated with gasses such as CO_2 and N_2. With their extraction from the reservoir, pressure and temperature decrease towards the extraction well. This disturbs the state of equilibrium the geothermal water is in with its dissolved components, which for gas can lead to exsolution. The exsolved gas bubbles can block the pores of the reservoir rock and therefore reduce the apparent permeability. As permeability reduction occurs mainly near the extraction well it can reduce production of geothermal waters substantially. This paper is aimed at experimentally investigating the conditions at which the onset of degassing starts and quantitatively assess any associated permeability decrease. Knowledge on these parameters will enable operators to adapt their operation procedures in order to ensure long-time reservoir permeability.

This paper reports core-flood experiments where tap water containing dissolved carbon dioxide was injected into either a Bentheimer (2.3 Darcy) or Berea (140 millidarcy) sandstone core at different conditions. The first sets of core-flood experiments showed that at a temperature of 30 °C and pressure up to 50 bars the onset of the degassing process correlates closely to CO_2 solubility values obtained by the Henry's law. At these conditions CO_2 degassing near the core outlet will cause the apparent permeability to decrease by a factor 2 to 5 in the high permeability Bentheimer sandstone core. At the same conditions the apparent permeability will decrease by a factor of nearly 10 in the low permeability Berea sandstone core. The decrease in effective permeability is gradual in the Bentheimer sandstone while in the Berea sandstone the change is steeper. For rocks with small pore sizes and low absolute permeability, the reduction in effective permeability is larger and the rate of permeability decrease is faster. However, the onset of degassing is not influenced by the pore size and initial permeability. Experiments at temperatures between 30 and 90 °C show that with increasing temperature, the Van 't Hoff equation becomes less to accurate to find the degassing pressure.

4.1 INTRODUCTION

Geothermal waters can have various gases in solution, such as CO_2, CH_4 and N_2. During the production of these waters, a change in pressure and temperature will occur in the vicinity of the extraction well. These changes disturb the equilibrium the water is in with its dissolved gases (Pátzay et al. (1998) and can result in various problems, such as degassing (Blöcher et al. (2016). The system then goes from single-phase flow (liquid) to two-phase flow (liquid and gas). The effective pore space available for the flow of water is reduced, as part of the total

pore space is taken up by gas. Therefore the effective permeability of the liquid phase will decrease (Bear, 2013).

This most likely occurred at the Groß Schönebeck geothermal site in Germany, where the productivity index (PI) dropped from 8.9 m^3/(h·MPa) to 0.6 m^3/(h·MPa), from June 2011 and November 2013. The decrease in permeability due the presence of free gas was proposed as a possible cause for the PI decline (Blöcher et al., 2016). Despite the many observations suggesting a direct link of PI decline and release of dissolved gas, data supporting this idea and a coherent picture about the process are lacking. This study aims to address the following question:

To what extent is the flow of water in rocks limited by release of free gas from a saturated water/gas solution?

by experimentally investigating at which conditions the onset of the degassing process starts and what the effect of the degassing process is on the effective water permeability. Factors influencing the degassing process and its effect on the permeability will be analyzed and discussed. These factors include the rock pore scale characteristics and temperature.

4.2   MATERIALS AND METHODS

This study comprises two series of core-flood experiments in which CO_2 and an aqueous phase were co-injected into a rock core. In the first series, two rocks samples were used, having either high permeability (Bentheimer sandstone, 2.3 D) or lower permeability (Berea sandstone, 140 mD). The temperature was set at 30 °C. The second series investigated a range of temperatures (up to 90 °C) and pressures (up to 80 bar) using only the low permeability core sample. This section outlines the experimental setup used in this study and the experimental procedure.

4.2.1 Experimental setup

Figure 19 shows a schematic of the experimental setup in these experiments. CO_2 supplied from a bottle was injected into the core using a gas booster and mass flow controller (Bronkhorst ELFLOW). The gas injection pressure was monitored using an absolute pressure transmitter (Keller PA33X, labelled p_1 in the schematic) is installed to monitor. A Quizix QX-1500 dual piston pump was used to inject the aqueous phase, here either tap water or 1M NaCl brine is used. Tap water was used instead of demineralized water to minimize the risk of the dissolution of clay particles from the cores. The rock core (40 cm long and 4 cm in diameter) is placed in a PEEK core holder, which is installed vertically in an oven that can be set to the desired temperature. Before reaching the rock core the fluids have to flow through a length of tubing in the oven (approximately 2 m in length). This allows them to reach the desired temperature and also gives the CO_2 time to mix with the water, such that only a single phase (water with dissolved CO_2) enters the core. The final length of tubing before the inlet of the core holder is transparent. This enables visual observation of the flowing fluids to ensure that the fluids are mixed properly before entering the core and no free gas bubbles are present. The fluids enter the core at the bottom, flow vertically through the core's pore space and exit at the top. A series of absolute pressure transmitters (Keller PA33X, p_2 to p_8 in the

schematic.) is installed along the length of the core that allow the monitoring of the pressure at various positions during the experiment. The desired operating pressure is set using a gas-controlled back-pressure regulator (Mity Mite S-91W) installed downstream of the core.
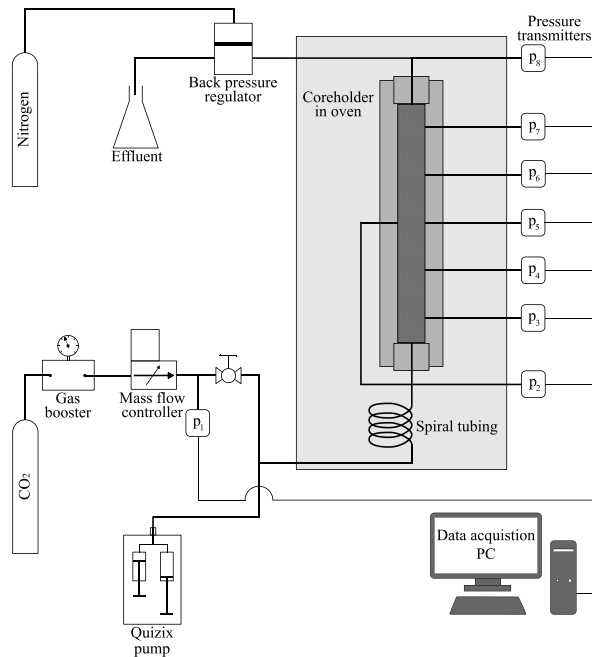

Figure 19: Schematic of experimental setup

4.2.2 Experimental procedure

The experiments carried out in this study are organized in several sets: each set consists of multiple experiments that aim to assess the influence of a particular variable (e.g. temperature or rock type) on the degassing process. By comparing two or more sets, the influence of these variables on the degassing process can be assessed. In each set, water and CO_2 are co-injected into the rock core.

The experiments discussed in this manuscript all use a gradually decreasing back-pressure to mimic the reducing reservoir pressure towards the production well. A similar procedure was used by (Zuo et al., 2012) in which a brine/CO_2 solution was depressurized during core-flood experiments. In each set, experiments were performed using various CO_2 concentrations. The initial back-pressure (*IBP*) was chosen sufficiently high such that the CO_2 fully dissolves in water. By lowering the back-pressure (*BP*), the point where the degassing starts, i.e. the degassing back-pressure (*DBP*), by monitoring the fluid pressure (*FP*) in the core. The formation of free gas is revealed by a significant rise of the of the *FP*.

Between each experiment the core is flushed with water to get the remaining CO_2 out. This is done by first lowering the backpressure, this causes gas expansion which forces the gas to leave the core. Then the backpressure is increased while injecting water, which results in a higher CO_2 solubility, thus causing the remaining CO_2 to dissolve in the water. Continuous flushing with water at elevated pressure allows for all of the CO_2 to be removed from the core making it ready for the next experiment.

4.2.3 Data analysis

The raw data obtained from each set of experiments consists essentially of the pressures measured at each pressure transducer taken at two second intervals. The difference between two adjacent pressure transducers combined with the difference in height gives the pressure gradient over an interval. To reduce the noise in the raw data it is edited using time averaging over 20 points. This improves the signal to noise ratio of the data significantly.

The results reported in this study are mostly pressure drops over the last section of the core as a function of the back-pressure. Since pressure is lowest in the last section degassing will start in this section. When a rapid increase of the pressure drop in the last section is observed, the *BP* measured at that point is taken as the onset of the degassing process or simply the degassing pressure (*DBP*).

The experimentally obtained *DBP* is then compared with the prediction of the bubble point from thermodynamic theory applied to the CO_2-water system. The bubble point pressure can be estimated using Henry's law (Eq. (2)).

$$ H_0 = \frac{s_{CO2}}{p} \tag{2} $$

where H_0 is the value of Henry's constant at standard conditions [equal to 0.336 mol/(L·bar) for CO_2], *p* is the pressure in bar and s_{CO2} is the solubility of CO_2 in water at standard conditions in mol/L (Sander, 2015). The solubility of gases in water typically decreases as the temperature increases. The applicability of Eq. (2) can be extended to higher temperatures by using the Van 't Hoff equation, which gives Henry's coefficient as function of the temperature *H*(*T*) as:

$$ H(T) = H_0 \exp\left[-\frac{\Delta_{sol}H}{R}\left(\frac{1}{T} - \frac{1}{T_0}\right)\right] \tag{3} $$

where the term $\Delta_{sol}H$ is the enthalpy of dissolution and T_0 is the reference temperature taken here as 298.15 K. $\Delta_{sol}H/R$ is independent of temperature and, for CO_2, is equal to 2400 K (Sander, 2015). The Van 't Hoff equation is used throughout this manuscript to compare the observed bubble points with the theoretical predictions. The observed pressure gradients can also be used to determine the effective core permeability by applying Darcy's law (Eq. (4)).

$$ k_{eff} = \frac{Q\mu_w L}{\Delta p_m} \tag{4} $$

where *Q* [m³/s]is the volumetric flux, μ_w [Pa·s] is the water viscosity at the investigated temperature, Δp_m [Pa] is the measured pressure drop, *L* [m] is the length of the investigated section of the core over which the pressure drop is measured and k_{eff} [m²]is the effective permeability of the medium based on the measured pressure drop. We have verified that for the flow rates used in this study the flow was in the laminar regime for which Darcy's law is valid.

4.3 RESULTS AND DISCUSSION

In this section, representative results of the experiments will be given and discussed. Since pressure is lowest towards the outlet of the core, this is the location where the first onset of degassing is expected to occur. This is why the results shown here are mostly pressure drops within this section. An overview of the conditions that were used for the various experiments is shown in Table 3.

Table 3: Overview of conditions used in the experiments.

Rock type	T [°C]	Aqueous phase	s_{CO2} [mol/L]
Bentheimer	30	Tap water	$0.85 - 1.3$
Berea	30	Tap water	$0.3 - 1.3$
Berea	$30 - 80$	Tap water	$0.2 - 0.4$

4.3.1 Onset of degassing

Figure 20 displays the steady-state pressure drop as a function of back-pressure, measured over the last core section for experiments using Bentheimer rock core at 30 °C. Each line corresponds to a different CO_2 concentration. Experiments start at high back-pressure (between 40 and 50 bar for these experiments) and then the back-pressure is lowered gradually. At the highest pressures, the pressure drop remains constant, indicating single phase flow without the formation of free gas. As the back-pressure decreased, at a certain degassing back-pressure (*DBP*), an increase in the pressure drop was observed. This is indicated by opaque markers in the figure. At pressures lower than the *DBP*, the pressure drop continued to increase thus indicating a reduced ability for the water to flow.
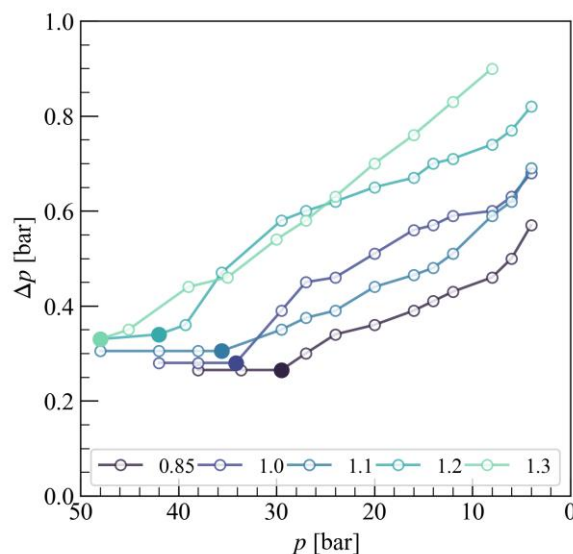

Figure 20: Pressure drop over the last interval of the core plotted against backpressure for experiments performed with different CO_2 concentrations displayed in the legend in mol/L. Opaque markers indicate the degassing back-pressure (*DBP*).

The *DBP* was compared to the theoretical solubility for CO_2 in water using Henry's law (Eq. [1]) combined with the Van 't Hoff equation (Eq. [2]) for a temperature of 30 °C. The experimentally obtained degassing points along with the theoretical prediction are given in Figure 21. Under the experimental conditions, we expect the Van 't Hoff equation to accurately predict the degassing pressure. This is largely confirmed by the data in Figure 21.
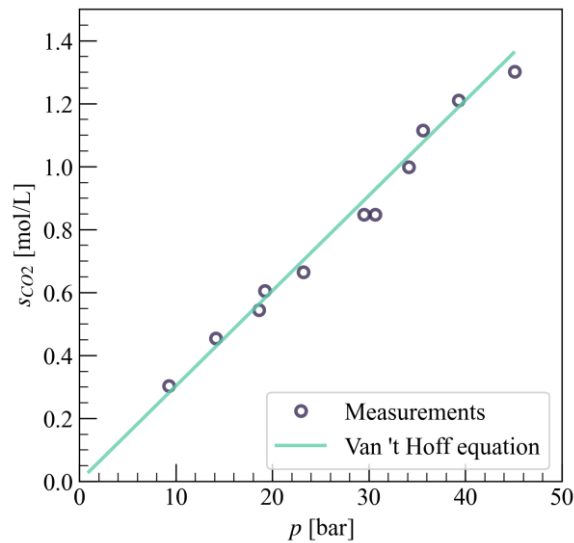

Figure 21: Measured *DBP* values for the degassing process (symbols) and their prediction using the Van 't Hoff equation (line)

Next, we assess the degree to which the effective permeability of the rock is reduced due to the presence of free gas bubbles. To this end, the pressure data from Figure 20 were used to determine the effective permeability corresponding to the degassing process by applying Eq. (4). The obtained effective permeabilities are shown in Figure 22 as a function of the back-pressure. Values in this manuscript have been normalized, i.e. the ratio of the effective permeability to the absolute permeability is plotted (k_{eff} / k_{abs}) The data show a gradual decrease in effective permeability for pressures lower than *DBP*. The permeability is reduced from its original absolute value of 2.3 D to between 0.8 and 1 D thus resulting in a reduction factor of 2.3 to 3.
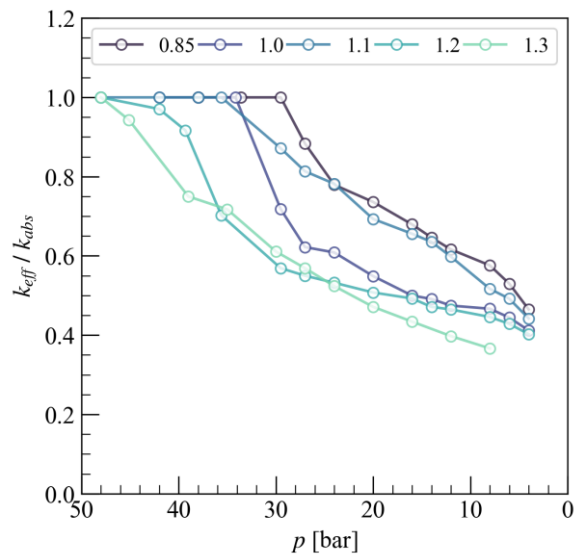
Figure 22: Effective permeability as a function of backpressure for experiments using a Bentheimer core performed with different CO_2 concentrations displayed in the legend [mol/L]

4.3.2 Effect of core lithology

Similar experiments were performed using a Berea rock core instead of Bentheimer to investigate the effect of lithology on the degassing process The Berea has a much lower initial permeability (0.14 D vs 2.3 D), which is caused by its smaller pores, literature reported average pore throat radii of 6 µm for the Berea vs 15 µm for Bentheimer (Al-Shakry et al., 2019). This affects the development of the effective permeability found in this study. Figure 23 shows the effective permeability as a function of the back-pressure for the Berea experiments.

The main takeaways are that the change between a state of single phase flow and that of blockage due to free gas formation is far more abrupt in the Berea compared to the more gradual transition found for the Bentheimer experiment. Also the extent to which the rock is blocked appears to be larger in the Berea with a decrease in effective permeability of roughly one order of magnitude (~100 à 10 mD) found for all CO_2 concentrations. This is interpreted to be a function of the kinetics of bubble growth. The Berea has more small pore throats what causes them to block earlier, because small bubbles already have the potential to block the pore throats while in the Bentheimer the small bubbles that form at the onset of the degassing process can still pass through the wider pore throats.
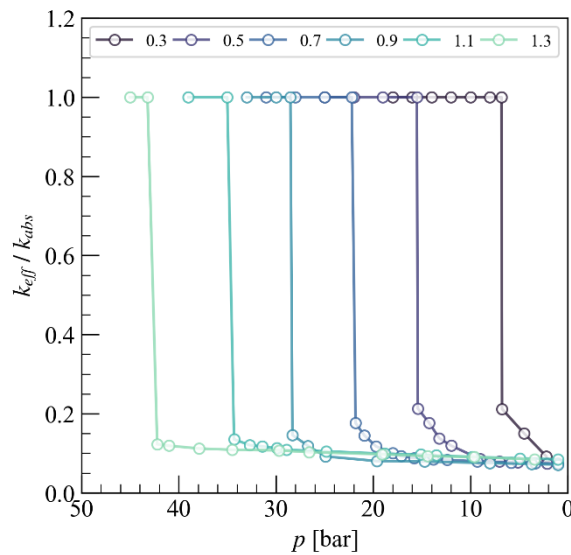
Figure 23: Effective permeability as a function of backpressure for experiments using a Berea core performed with different CO_2 concentrations displayed in the legend [mol/L]

Figure 24 shows a direct comparison of the reduction the effective permeabilities found in the Bentheimer and Berea experiments at pressures below the bubble point. This reinforces the finding in Figure 23 that the change in effective permeability happens much more abrupt for the Berea rock than the Bentheimer. At pressures just a few bars below the onset of degassing, already a 82% reduction in permeability is found for the Berea, which rises to 91% as the pressure is reduced further. As mentioned in the introduction, (Blöcher et al., 2016) found a reduction of the productivity index of approximately 93% for the Groß Schönebeck reservoir, which is similar in magnitude as the reduction in effective permeability found here for the Berea sandstone. For the Bentheimer, the change is much more gradual and even at pressures 25 bars below the onset of degassing only a reduction of 48% is achieved.
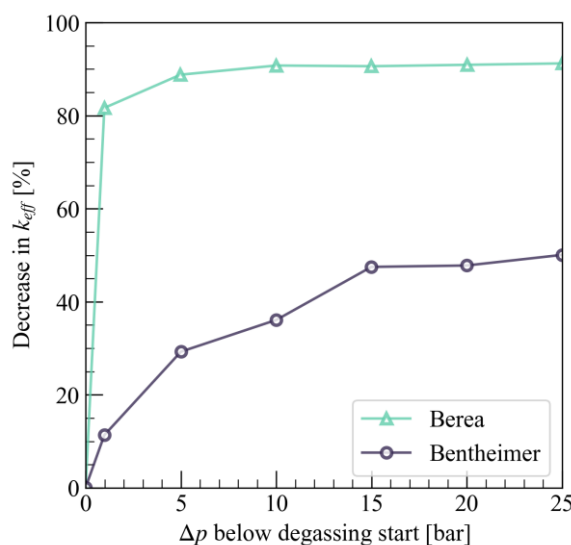

Figure 24: Comparison of the reduction in effective permeability (percentage) after the degassing process has started for the Berea and Bentheimer sandstone cores

4.3.3 Effect of temperature

In the second series, the influence of temperature has been investigated by repeating the experiments on Berea sandstone at a range of temperatures (30–90 °C). The resulting effective permeabilities at these temperatures for the Berea experiment are shown in Figure 25. The CO_2 concentration used here is kept at the same value of 0.4 mol/L for all investigated temperatures. Some differences in the initial permeability is found, especially for the 80 °C experiment which has a significantly higher permeability compared to the experiments at lower temperatures. A possible reason for this is that at high temperatures the PEEK core holder can become slightly ductile thereby creating a non-ideal connection between the core holder and the pressure transducer that can lead to errors in the pressure measurements. For each experiment, the effective permeability was calculated using the viscosity of water at the set temperature (Korson et al., 1969).

Higher temperatures lead to increased degassing pressures, which is to be expected due to reduced solubility. The extent to which the effective permeability is reduced is not a strong function of the temperatures, with similar values of reduction found for all investigated temperatures. For example, the 70 °C experiment showed a final reduction of 89% in permeability vs. 91% for the 30 °C experiment.
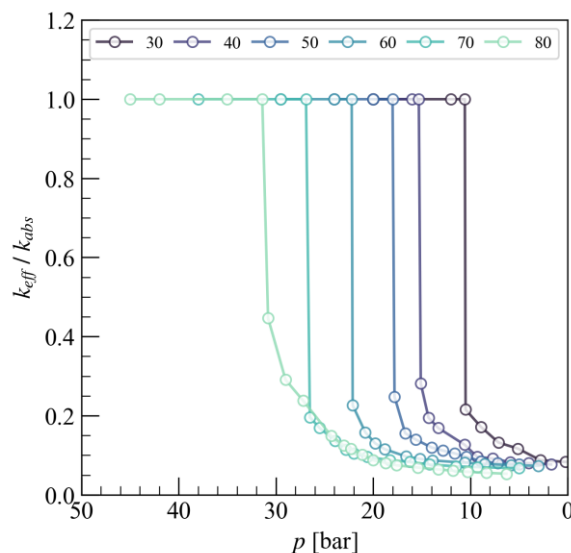

Figure 25: Comparison of the effective permeability for experiments performed at different temperatures. Legend indicates used temperature [°C]

Another set of experiments with a range of different temperatures was performed using a lower CO_2 concentration of 0.2 mol/L. The value of the degassing pressures here were lower compared to the experiments using 0.4 mol/L, but the trend that higher temperatures lead to higher degassing pressures was also found here. Both sets of experiments were also compared to the theoretical CO_2 solubility limit according to the Van 't Hoff equation. Figure 26 shows the experimentally obtained degassing pressures as a function of the temperature for both sets of experiments along with the theoretical prediction. For all temperatures, the experimentally obtained degassing pressure is lower than the theoretical prediction with higher temperatures lead to larger deviations from theory. A possible reason for this discrepancy is that the theoretical curves were created using a value of 2400 K for the enthalpy

of dissolution (the term $\Delta_{sol}H/R$ in Eq. (3)). This value is debatable and values ranging from 2200 to 2900 are found in literature (Sander, 2015).
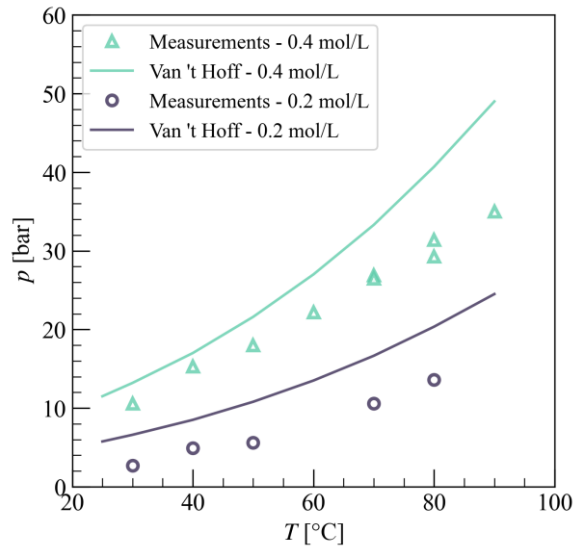

Figure 26: Onset degassing pressure as a function of temperature for experiments with a fixed CO_2 concentration of 0.2 and 0.4 mol/L along with model prediction according to the Van 't Hoff equation

4.4   CONCLUSIONS

At temperatures of 30 °C and moderate pressures (up to 50 bar), the maximum CO_2 solubility in water according to Henry's law gives a good indication for when the degassing process starts. This applicability can be extended to higher temperatures using the Van 't Hoff equation, although increased deviations from theory were found at higher temperature regimes. The effect of the degassing process on the effective permeability of a rock is largely influenced by the pore scale characteristics of a rock. Comparing a high permeable (2.3 Darcy) Bentheimer sandstone core with a lower permeable (0.14 Darcy) Berea sandstone core shows that the degassing process causes the effective permeability to reduce faster in the low permeable Berea core than in the Bentheimer core. The total decrease in effective permeability in the Berea core is also significantly higher than in the Bentheimer core: 91% vs. 48% respectively for the experiment at 30 °C. This difference is most likely due their difference in pore throat size distribution.

The extent to which the effective permeability is reduced by the formation of free gas is only very slightly affected by temperature. By increasing the temperature, the total decrease in effective permeability due to degassing went from 91% to 89% at 30 and 70 °C respectively.

5   CONCLUDING REMARKS

REFLECT Task 1.3 has resulted in an improved understanding of the physical principles of the degassing process for CO_2-water mixtures and its implications for flow in both bulk and porous media. Results presented in this report have been disseminated either through journal publication or presentations at conferences.

A high-pressure visual cell has been designed and constructed specifically for this task. This cell is made of corrosion resistant titanium and uses sapphire windows through which its inner volume can be monitored. In its current state, this apparatus is able to function at pressures up to 200 bar and temperatures up to 200 °C.

Depressurization experiments using this visual cell have led to the following conclusions for degassing of CO_2-water mixtures in bulk. Under moderate conditions, when CO_2 is in a gaseous state, the formation of the first free gas bubbles is in reasonable agreement with the Van 't Hoff equation, which dictates the solubility of gases at elevated temperatures. However, increased deviations were found when using higher temperatures. Improved predictions can be established using other equations of state (e.g. (Duan and Sun, 2003)), although deviations up to several bars still persist. Employing higher initial pressures, such that CO_2 is in its supercritical state, resulted in a significant reduction in the measured bubble point pressure. The measured bubble points are up to 50% lower compared to the theoretical prediction using the Van 't Hoff equation. Several possible explanations have been explored that could cause the dependency of the bubble point on the initial state of the experiments. These include parameters such as the rate of depressurization and the use of a different visual cell, along with a thorough analysis of differences in bubble kinetics between the various experiments. This sensitivity analysis provided no clear indication that these parameters could have a significant impact on the bubble point.

The degassing experiments in porous media show that at temperatures of 30 °C and moderate pressures (up to 50 bar), the maximum CO_2 solubility in water according to Henry's law gives a good indication for the pressure below which free gas starts to form. This applicability can be extended to higher temperatures using the Van 't Hoff equation, although increased deviations from theory were found at higher temperature regimes. Comparing a high and lower permeability core (Bentheimer vs. Berea) shows that the formation of free gas causes the effective permeability to reduce faster in the Berea core than in the Bentheimer core at pressures below the bubble point. A drop in effective permeability up to 91% was found for the Berea core, which is significantly higher than the 48% drop in the Bentheimer core for the experiment at 30 °C. This difference is most likely due their difference in pore throat size distribution, with the free gas bubbles immediately blocking the narrower throats in the Berea rock. Performing experiments at higher temperatures causes the degassing process to start at a higher pressure due to reduced CO_2 solubility. However, the extent to which the effective permeability is altered is very similar to previous experiments at lower temperatures.

LIST OF PUBLICATIONS

Boeije, C.S., Zitha, P.L.J. and Pluymakers, A.H.M., "Experimental investigation of degassing properties of geothermal fluids", presented at EGU General Assembly 2021, Vienna, Austria, 19 – 30 April 2021

Boeije, C.S., Verweij, C., Zitha, P.L.J. and Pluymakers, A.H.M., "CO_2 degassing kinetics in porous media", presented at InterPore2022, 14th Annual Meeting, Abu Dhabi, United Arab Emirates, 30 May – 2 June 2022

Boeije, C.S., Verweij, C., Zitha, P.L.J. and Pluymakers, A.H.M., "CO_2 degasssing of geothermal fluids during core-flood experiments", presented at European Geothermal Congress 2022, Berlin, Germany, 17 – 21 October 2022

Boeije, C.S., Zitha, P.L.J. and Pluymakers, A.H.M., "High speed imaging of degassing kinetics of CO_2-water mixtures", Physics of Fluids **34**, 123307 (2022), https://doi.org/10.1063/5.0124500

REFERENCES

Aiuppa, A., C. Federico, G. Giudice, S. Gurrieri, M. Liuzzo, H. Shinohara, R. Favara, and M. Valenza, 2006, Rates of carbon dioxide plume degassing from Mount Etna volcano: Journal of Geophysical Research: Solid Earth, v. 111.

Al-Shakry, B., B. Shaker Shiran, T. Skauge, and A. Skauge, 2019, Polymer Injectivity: Influence of Permeability in the Flow of EOR Polymers in Porous Media, SPE Europec featured at 81st EAGE Conference and Exhibition, p. D032S013R004.

Arnórsson, S., 1989, Deposition of calcium carbonate minerals from geothermal waters — theoretical considerations: Geothermics, v. 18, p. 33-39.

Baranenko, V. I., V. S. Sysoev, L. N. Fal'kovskii, V. S. Kirov, A. I. Piontkovskii, and A. N. Musienko, 1990, The solubility of nitrogen in water: Soviet Atomic Energy, v. 68, p. 162-165.

Barták, J., 1990, A study of the rapid depressurization of hot water and the dynamics of vapour bubble generation in superheated water: International Journal of Multiphase Flow, v. 16, p. 789-798.

Bear, J., 2013, Dynamics of Fluids in Porous Media, Dover Publications.

Blöcher, G., T. Reinsch, J. Henninges, H. Milsch, S. Regenspurg, J. Kummerow, H. Francke, S. Kranz, A. Saadat, G. Zimmermann, and E. Huenges, 2016, Hydraulic history and current state of the deep geothermal reservoir Groß Schönebeck: Geothermics, v. 63, p. 27-43.

Bornemann, T. L. V., P. S. Adam, V. Turzynski, U. Schreiber, P. A. Figueroa-Gonzalez, J. Rahlff, D. Köster, T. C. Schmidt, R. Schunk, B. Krauthausen, and A. J. Probst, 2020, Geological degassing enhances microbial metabolism in the continental subsurface: bioRxiv, p. 2020.03.07.980714.

Caracausi, A., F. Italiano, A. Paonita, A. Rizzo, and P. M. Nuccio, 2003, Evidence of deep magma degassing and ascent by geochemistry of peripheral gas emissions at Mount Etna (Italy): Assessment of the magmatic reservoir pressure: Journal of Geophysical Research: Solid Earth, v. 108.

Carvalho, P. J., L. M. C. Pereira, N. P. F. Gonçalves, A. J. Queimada, and J. A. P. Coutinho, 2015, Carbon dioxide solubility in aqueous solutions of NaCl: Measurements and modeling with electrolyte equations of state: Fluid Phase Equilibria, v. 388, p. 100-106.

Chiodini, G., A. Baldini, F. Barberi, M. L. Carapezza, C. Cardellini, F. Frondini, D. Granieri, and M. Ranaldi, 2007, Carbon dioxide degassing at Latera caldera (Italy): Evidence of geothermal reservoir and evaluation of its potential energy: Journal of Geophysical Research: Solid Earth, v. 112.

Cho, H., J. Kim, and K.-H. Han, 2019, An assembly disposable degassing microfluidic device using a gas-permeable hydrophobic membrane and a reusable microsupport array: Sensors and Actuators B: Chemical, v. 286, p. 353-361.

Cosmo, R. d. P., F. d. A. Ressel Pereira, D. d. C. Ribeiro, W. Q. Barros, and A. L. Martins, 2019, Estimating CO2 degassing effect on CaCO3 precipitation under oil well conditions: Journal of Petroleum Science and Engineering, v. 181, p. 106207.

Delale, C. F., J. Hruby, and F. Marsik, 2002, Homogeneous bubble nucleation in liquids: The classical theory revisited: The Journal of Chemical Physics, v. 118, p. 792-806.

dos Santos, P. F., L. André, M. Ducousso, A. Lassin, F. Contamine, A. Lach, M. Parmentier, and P. Cézac, 2021, An improved model for CO2 solubility in aqueous Na+–Cl−–SO42− systems up to 473.15 K and 40 MPa: Chemical Geology, v. 582, p. 120443.

Duan, Z., and R. Sun, 2003, An improved model calculating CO2 solubility in pure water and aqueous NaCl solutions from 273 to 533 K and from 0 to 2000 bar: Chemical Geology, v. 193, p. 257-271.

Eskin, D., N. Alba-Baena, T. Pabel, and M. da Silva, 2015, Ultrasonic degassing of aluminium alloys: basic studies and practical implementation: Materials Science and Technology, v. 31, p. 79-84.

Eskin, D. G., 2015, 20 - Ultrasonic degassing of liquids, *in* J. A. Gallego-Juárez, and K. F. Graff, eds., Power Ultrasonics: Oxford, Woodhead Publishing, p. 611-631.

Frondini, F., S. Caliro, C. Cardellini, G. Chiodini, and N. Morgantini, 2009, Carbon dioxide degassing and thermal energy release in the Monte Amiata volcanic-geothermal area (Italy): Applied Geochemistry, v. 24, p. 860-875.

Fu, Y., W. van Berk, and H.-M. Schulz, 2013, Temporal and spatial development of scale formation: One-dimensional hydrogeochemical transport modeling: Journal of Petroleum Science and Engineering, v. 112, p. 273-283.

Garven, G., 2015, Fault-Related CO_2 Degassing, Geothermics, and Fluid Flow in Southern California Basins--Physiochemical Evidence and Modeling, United States.

Groth, T., A. Luke, D. Mewes, and M. Reichwage, 2009, Effects of Dissolving and Degassing Phenomena on Multiphase Oil and Gas Boosting.

Gyarmati, G., G. Fegyverneki, M. Tokár, and T. Mende, 2021, The Effects of Rotary Degassing Treatments on the Melt Quality of an Al–Si Casting Alloy: International Journal of Metalcasting, v. 15, p. 141-151.

Haizlip, J., M. Stover, S. Garg, F. Tut Haklidir, and N. Prina, 2016, Origin and Impacts of High Concentrations of Carbon Dioxide in Geothermal Fluids of Western Turkey: 41st Workshop on Geothermal Reservoir Engineering.

Henley, R. W., A. H. Truesdell, P. B. Barton, Jr., and J. A. Whitney, 1984, Fluid-Mineral Equilibria in Hydrothermal Systems, Society of Economic Geologists.

Ivannikov, V. I., I. V. Ivannikov, and T. W. Bakker, 2003, Production Improvement By Controlling The Flow Regime Of Gas Rich Fluid Mixtures With Slugging Devices.

Karlsson, J. M., M. Gazin, S. Laakso, T. Haraldsson, S. Malhotra-Kumar, M. Mäki, H. Goossens, and W. van der Wijngaart, 2013, Active liquid degassing in microfluidic systems: Lab on a Chip, v. 13, p. 4366-4373.

Korson, L., W. Drost-Hansen, and F. J. Millero, 1969, Viscosity of water at various temperatures: The Journal of Physical Chemistry, v. 73, p. 34-39.

Kumzerova, E. Y., and A. A. Schmidt, 2002, A numerical simulation of nucleation and dynamics of bubbles formed under drastic depressurization of a liquid: Technical Physics, v. 47, p. 829-833.

Lara Cruz, J., E. Neyrolles, F. Contamine, and P. Cézac, 2021, Experimental Study of Carbon Dioxide Solubility in Sodium Chloride and Calcium Chloride Brines at 333.15 and 453.15 K for Pressures up to 40 MPa: Journal of Chemical & Engineering Data, v. 66, p. 249-261.

Li, J., L. Wei, and X. Li, 2014, Modeling of CO2-CH4-H2S-brine based on cubic EOS and fugacity-activity approach and their comparisons: Energy Procedia, v. 63, p. 3598-3607.

Liger-Belair, G., 2005, The Physics and Chemistry behind the Bubbling Properties of Champagne and Sparkling Wines: A State-of-the-Art Review: Journal of Agricultural and Food Chemistry, v. 53, p. 2788-2802.

Liger-Belair, G., 2019, Carbon Dioxide in Bottled Carbonated Waters and Subsequent Bubble Nucleation under Standard Tasting Condition: Journal of Agricultural and Food Chemistry, v. 67, p. 4560-4567.

Liger-Belair, G., F. Sternenberg, S. Brunner, B. Robillard, and C. Cilindre, 2015, Bubble dynamics in various commercial sparkling bottled waters: Journal of Food Engineering, v. 163, p. 60-70.

Meadley, S. L., and F. A. Escobedo, 2012, Thermodynamics and kinetics of bubble nucleation: Simulation methodology: The Journal of Chemical Physics, v. 137, p. 074109.

Meng, D. D., J. Kim, and C.-J. Kim, 2006, A degassing plate with hydrophobic bubble capture and distributed venting for microfluidic devices: Journal of Micromechanics and Microengineering, v. 16, p. 419-424.

Park, S., H. Cho, J. Kim, and K.-H. Han, 2021, Lateral Degassing Method for Disposable Film-Chip Microfluidic Devices: Membranes, v. 11.

Pátzay, G., G. Stáhl, F. H. Kármán, and E. Kálmán, 1998, Modeling of scale formation and corrosion from geothermal water: Electrochimica Acta, v. 43, p. 137-147.

Peiffer, L., G. Carrasco-Núñez, A. Mazot, R. E. Villanueva-Estrada, C. Inguaggiato, R. Bernard Romero, R. Rocha Miller, and J. Hernández Rojas, 2018, Soil degassing at the Los Humeros geothermal field (Mexico): Journal of Volcanology and Geothermal Research, v. 356, p. 163-174.

Puga, H., J. Barbosa, J. Gabriel, E. Seabra, S. Ribeiro, and M. Prokic, 2011, Evaluation of ultrasonic aluminium degassing by piezoelectric sensor: Journal of Materials Processing Technology, v. 211, p. 1026-1033.

Qin, Z., M. Arshadi, and M. Piri, 2021, Carbonated Water Injection and In Situ CO2 Exsolution in Oil-Wet Carbonate: A Micro-Scale Experimental Investigation: Energy & Fuels, v. 35, p. 6615-6632.

Rodríguez, F., N. M. Pérez, G. V. Melián, E. Padrón, P. A. Hernández, M. Asensio-Ramos, G. D. Padilla, J. Barrancos, and L. D'Auria, 2021, Exploration of deep-seated geothermal reservoirs in the Canary Islands by means of soil CO2 degassing surveys: Renewable Energy, v. 164, p. 1017-1028.

Sander, R., 2015, Compilation of Henry's law constants (version 4.0) for water as solvent: Atmos. Chem. Phys., v. 15, p. 4399-4981.

Sbrana, A., P. Marianelli, M. Belgiorno, M. Sbrana, and V. Ciani, 2020, Natural CO2 degassing in the Mount Amiata volcanic–geothermal area: Journal of Volcanology and Geothermal Research, v. 397, p. 106852.

Shaayegan, V., G. Wang, and C. B. Park, 2016, Study of the bubble nucleation and growth mechanisms in high-pressure foam injection molding through in-situ visualization: European Polymer Journal, v. 76, p. 2-13.

Shafer, N. E., and R. N. Zare, 1991, Through a Beer Glass Darkly: Physics Today, v. 44, p. 48-52.

Shen, L., K. Wu, Q. Xiao, and D. Yuan, 2011, Carbon dioxide degassing flux from two geothermal fields in Tibet, China: Chinese Science Bulletin, v. 56, p. 3783-3793.

Smith, F. L., 2007, Environmental Management Where do Henry's constants come from?

Stefánsson, A., N. S. Keller, J. G. Robin, H. Kaasalainen, S. Björnsdóttir, S. Pétursdóttir, H. Jóhannesson, and G. Ó. Hreggvidsson, 2016, Quantifying mixing, boiling, degassing, oxidation and reactivity of thermal waters at Vonarskard, Iceland: Journal of Volcanology and Geothermal Research, v. 309, p. 53-62.

Taweelarp, S., S. Suntikoon, T. Rojsiraphisal, N. Ploymaklam, and S. Saenton, 2021, Geochemical Modeling of Scale Formation due to Cooling and CO2-degassing in San Kamphaeng Geothermal Field, Northern Thailand: Chiang Mai University Journal of Natural Sciences, v. 20.

Uzel, S., M. A. Chappell, and S. J. Payne, 2006, Modeling the Cycles of Growth and Detachment of Bubbles in Carbonated Beverages: The Journal of Physical Chemistry B, v. 110, p. 7579-7586.

Wang, C., 2022, Bubble Dynamics in High-Pressure Foam Injection Molding, University of Toronto (Canada).

Xu, X., D. E. Cristancho, S. Costeux, and Z.-G. Wang, 2013, Bubble nucleation in polymer–CO2 mixtures: Soft Matter, v. 9, p. 9675-9683.

Zenit, R., and J. Rodríguez-Rodríguez, 2018, The fluid mechanics of bubbly drinks: Physics Today, v. 71, p. 44-50.

Zhao, H., M. V. Fedkin, R. M. Dilmore, and S. N. Lvov, 2015, Carbon dioxide solubility in aqueous solutions of sodium chloride at geological conditions: Experimental results at 323.15, 373.15, and 423.15K and 150bar and modeling up to 573.15K and 2000bar: Geochimica et Cosmochimica Acta, v. 149, p. 165-189.

Zuo, L., S. Krevor, R. W. Falta, and S. M. Benson, 2012, An Experimental Study of CO2 Exsolution and Relative Permeability Measurements During CO2 Saturated Water Depressurization: Transport in Porous Media, v. 91, p. 459-478.